

The meaning of *WISE* colours – I. The Galaxy and its satellites

Robert Nikutta,^{1,2*} Nicholas Hunt-Walker,³ Maia Nenkova,⁴ Željko Ivezić³ and Moshe Elitzur²

¹*Departamento de Ciencias Físicas, Universidad Andrés Bello, Av. República 252, Santiago, Chile*

²*Department of Physics & Astronomy, University of Kentucky, Lexington, KY 40506, USA*

³*Astronomy Department, University of Washington, Box 351580, Seattle, WA 98195-1580, USA*

⁴*School of English and Liberal Studies, Seneca College, Toronto, ON, M2J 2X5, Canada*

Version of 3 July 2014

ABSTRACT

Through matches with the Sloan Digital Sky Survey (SDSS) catalogue we identify the location of various families of astronomical objects in *WISE* colour space. We identify reliable indicators that separate Galactic/local from extragalactic sources and concentrate here on the objects in our Galaxy and its closest satellites. We develop colour and magnitude criteria that are based only on *WISE* data to select asymptotic giant branch (AGB) stars with circumstellar dust shells, and separate them into O-rich and C-rich classes. With these criteria we produce an all-sky map for the count ratio of the two populations. The map reveals differences between the Galactic disc, the Magellanic Clouds and the Sgr Dwarf Spheroidal galaxy, as well as a radial gradient in the Large Magellanic Cloud (LMC) disc. We find that the C:O number ratio for dusty AGB stars increases with distance from the LMC centre about twice as fast as measured for near-IR selected samples of early AGB stars. Detailed radiative transfer models show that *WISE* colours are well explained by the emission of centrally heated dusty shells where the dust has standard properties of interstellar medium (ISM) grains. The segregation of different classes of objects in *WISE* colour space arises from differences in properties of the dust shells: those around young stellar objects have uniform density distributions while in evolved stars they have steep radial profiles.

Key words: radiative transfer – stars: AGB and post-AGB – Galaxy: structure – Magellanic Clouds – infrared: general – infrared: stars.

1 INTRODUCTION

Infrared emission from radiatively heated dust carries important information about the distribution of material around the heating source. This information can be deciphered either through detailed imaging and analysis of the spectral energy distribution (SED) of individual objects, or by studying the SED properties (such as colours) of statistically large populations of sources. The pioneering *Infrared Astronomical Satellite* (*IRAS*; launched in 1983) all-sky survey ushered in the era of modern highly successful astronomical surveys (Neugebauer et al. 1984; Olmon et al. 1986). The *IRAS* survey provided unprecedented opportunity to classify the infrared properties of about 350 000 astronomical objects using a homogeneous data set obtained with a single facility (e.g. van der Veen & Habing 1988). Thanks to sensitivity improvements of up to three orders of magnitude compared to *IRAS*, the recent *Wide-field Infrared Survey Explorer* (*WISE*; launched in 2010) all-sky survey

detected about 560 million objects (Wright et al. 2010). *WISE* represents the next major step in surveying and understanding of the infrared sky. For example, data from the *IRAS* point source catalogue (PSC) showed that certain Galactic objects tend to cluster in well-defined regions of *IRAS* colour–colour (CC) diagrams, and the same clustering is expected in the *WISE* photometric system but for a significantly larger sample that probes a much larger volume of the Galaxy. Furthermore, and perhaps more importantly, *WISE* data are deep enough for its catalogues to contain a very large number of extragalactic sources, and they too are clustered in well-defined regions of *WISE* CC and colour–magnitude (CM) diagrams. Although *IRAS*, too, detected some extragalactic objects (for a review see Soifer et al. 1987), *WISE* can be considered a true IR counterpart to modern optical surveys of extragalactic sources, such as the Sloan Digital Sky Survey (SDSS; York et al. 2000).

WISE mapped the sky at 3.4, 4.6, 12, and 22 μm with an angular resolution of 6.1, 6.4, 6.5 and 12.0 arcsec, respectively. Fig. 1 shows the *WISE* bandpasses and their comparison to other major infrared surveys. Throughout this paper we will refer to the filter names as ‘W1 filter’ (and W2, W3, and W4 filters). The source

* E-mail: robert.nikutta@gmail.com

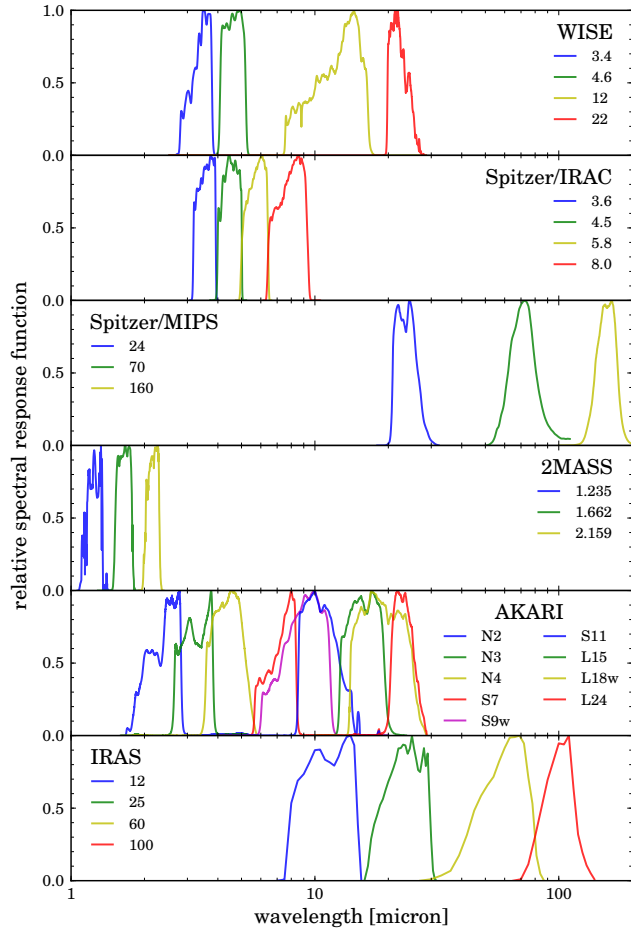


Figure 1. A comparison of bandpass filters for *WISE* and other major infrared surveys. From top to bottom: *WISE*, *Spitzer/IRAC*, *Spitzer/MIPS*, *2MASS*, *AKARI*, *IRAS*. *2MASS* is the only ground-based survey. The central filter wavelengths (in micron) or the established filter names are given in the legends.

SED λF_λ is averaged in each band by the instrument’s transmission function $W_i(\lambda)$, where $i = 1, 2, 3, 4$. This yields the in-band fluxes $F_i = \int W_i(\lambda) \cdot \lambda F_\lambda d\lambda$. The *WISE* Catalogue provides magnitudes calibrated in the Vega system using an empirical fit to the Vega spectrum (see equation 2 in [Wright et al. 2010](#)). Thus the calibrated in-band fluxes are

$$f_i = \frac{F_i}{F_i^{\text{Vega}}} = \frac{\int W_i(\lambda) \cdot \lambda F_\lambda d\lambda}{\int W_i(\lambda) \cdot \lambda F_\lambda^{\text{Vega}} d\lambda}. \quad (1)$$

‘Colour’ is the magnitude difference between two measured fluxes of an astronomical source, e.g., $W1 - W2 = 2.5 \log(f_2/f_1)$ for bands 1 and 2. We will also use the short-hand notation W12 for such colour.

WISE attained 5σ point-source sensitivities better than 0.068, 0.098, 0.86 and 5.4 mJy in the W1 through W4 bands, respectively, which correspond to Vega-based magnitudes 16.83, 15.6, 11.32 and 8.0¹. These survey sensitivity limits apply in unconfused regions on the Ecliptic; they improve towards the ecliptic poles due

to denser coverage and a lower zodiacal background. Photometric measurements of sources brighter than approximately 8.1, 6.7, 3.8 and -0.4 mag (Vega) are affected by saturation of the detectors. The astrometric precision for sources brighter than $\text{SNR}=40$ is about 0.2 arcsec.

The *WISE* All-Sky Release comprises all data taken during the full cryogenic mission phase (2010 January 7 to 2010 August 6). It includes an Atlas of 18 240 images, a Source Catalogue with positional and photometric data for over 563 million objects, and also an Explanatory Supplement. Unlike *IRAS* catalogues which reported fluxes in Jansky, *WISE* measurements are reported on the Vega magnitude scale. Although this difference makes a direct comparison with some *IRAS*-based studies more difficult, we follow already published work based on *WISE* data and use unaltered catalogued Vega-based magnitudes. A more detailed discussion can be found in [Wright et al. \(2010\)](#) and at the *WISE* data release website².

[Wright et al. \(2010\)](#) have demonstrated that *WISE* detected all the main families of extragalactic sources, including star-forming (SF) galaxies, galaxies with active nuclei (AGN) and quasars (QSO). Their positions in a representative *WISE* CC diagram are shown schematically in the left panel of Fig. 2, and the challenge to theory is to come up with an explanation as to why different types of objects segregate the way they do. Similar structuring has been observed in *IRAS*-based CC diagrams; its details were explained by [Ivezić & Elitzur \(2000\)](#). The colours of a ‘naked’ radiation source correspond to a point in colour space; since *WISE* colours are normalized to Vega, colours of blackbody emission are close to 0. Embedding the source in a dust shell, the radiation is reprocessed to longer wavelengths and the colours are shifted to the red. The larger is the dust optical thickness, the redder are the colours. Therefore, increasing the shell optical depth while keeping all its other properties constant produces a track in CC diagrams with distance from the origin along the track increasing with optical depth. The right panel of Fig. 2 shows for illustration three tracks produced by spherical ISM-dust shells with power-law radial density distributions of varying steepness. The tracks for uniform density and for $1/r$ density falloff nicely outline the boundaries of the region occupied by stars and extragalactic sources in the *WISE* CC diagram. Similarly, the *WISE* colours produced by clumpy torus models ([Nenkova et al. 2008a,b](#)), shown as grey-scale number density distribution, match the region of QSO and Seyferts. Our aim is to present in this paper a more detailed analysis of *WISE* colours of sources in the Galaxy and its satellites, and in a companion paper for AGN and quasars ([Nikutta et al., in preparation](#)).

We begin this first paper by identifying the *WISE* colours of families of astronomical sources through matching with the SDSS catalogue. The matching criteria and their results are described in Section 2. In particular, almost 40 million *WISE* sources are matched with Galactic stars, and in Section 3 we concentrate on the nature of these stellar sources. We proceed to calculate model colour tracks for the *WISE* photometric system which can be used to interpret the observed clustering of different stellar populations in the CC diagrams. The models and their comparison to *WISE* data are described in detail in Section 4. Our results are summarized and discussed in Section 5.

¹ See the *WISE* Explanatory Supplement: <http://wise2.ipac.caltech.edu/docs/release/allsky/expsup/>

² See: <http://wise2.ipac.caltech.edu/docs/release/allsky/>

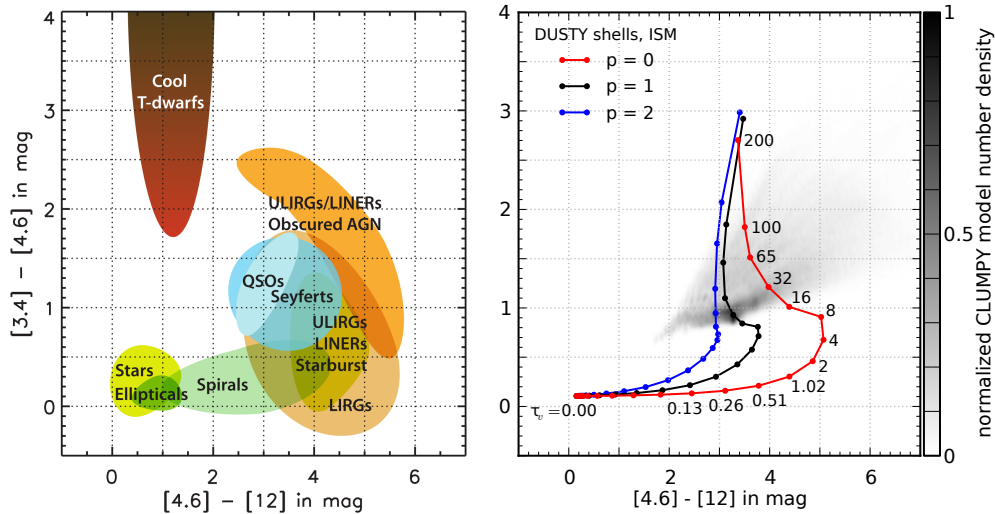


Figure 2. Qualitative comparison of *WISE* colours with models. Left: schematic distribution of *WISE* colours for various families of astronomical sources. This is fig. 12 from Wright et al. (2010), reproduced with permission of the authors and AAS. Right: sample model predictions for standard ISM dust. Solid lines show colour tracks for IR emission from dusty spherical shells that are centrally heated by a 5000 K blackbody point source to a dust temperature of 1000 K on the shell inner boundary. The shell radial density profile is r^{-p} , with $p = 0, 1$ and 2 shown in red, black and blue tracks, respectively. Positions along each track correspond to the shell optical depth at visual, as marked on the red track. Results of AGN clumpy torus models (see Nikutta et al., in preparation) are shown as a grey-scale number density distribution normalized to its peak value.

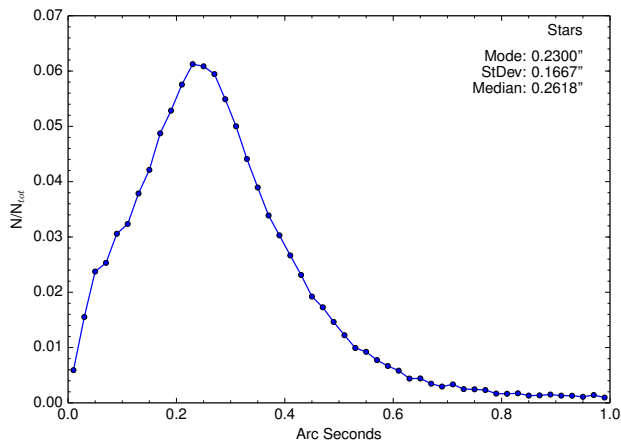


Figure 3. Distribution of matching radii (in arcsec) between *WISE* and SDSS for our sample of stars. Based on this figure we adopt a matching radius of 1 arcsec in this paper.

2 SDSS MATCHES FOR *WISE* OBJECTS

To enable a quantitative identification of source populations and subsequent comparison with our models, we use a sub-sample of *WISE* sources with SDSS-based identifications for five types of object: quasars, galaxies classified as AGN, SF and luminous red galaxies (LRG; essentially elliptical galaxies), and stars (optically unresolved objects not in the quasar sample). We first employ positional matching within a 1.0 arcsec radius of the *WISE* All-sky Data Release Catalogue, using procedures described in Obrić et al. (2006) and Covey et al. (2007): we match with SDSS Data Release 7 Catalogue for samples with spectroscopy, and Data Release 8 for unresolved sources in imaging data. The 1 arcsec cutoff matching radius is well justified. Fig. 3 shows the distribution of matching radii between *WISE* and SDSS for our sample of stars: the median

and standard deviation are 0.26 ± 0.17 arcsec. For a sample of LRGs and star forming galaxies (not shown) it is 0.52 ± 0.26 arcsec. After positional matching, we enforce quality cuts for *WISE* photometry, as described further below. Fig. 4 shows three representative *WISE* CM diagrams for the five sub-samples selected as follows.

- *Quasars*: starting with 98 047 sources from the SDSS catalogue of quasars (Schneider et al. 2010) that have a *WISE* source closer than 1 arcsec, we further require that all four *WISE* magnitudes are brighter than 5σ limits and have a reliably measured uncertainty, yielding a sample of 14 795 quasars.
- *Star forming and AGN galaxies*: Galaxies with SDSS spectra are selected from the NYU VAGC Catalogue³ (Blanton et al. 2005). Galaxies with spectral emission lines are further classified as SF and AGN galaxies using the Baldwin-Phillips-Terlevich diagram (Baldwin et al. 1981). There are 12 379 AGN and 180 329 SF galaxies within 1 arcsec of a *WISE* source. The cuts for their *WISE* photometry are the same as for quasars, yielding samples of 4509 AGN and 38 092 SF galaxies.
- *LRGs*: luminous red galaxies are adopted from a catalogue constructed for cosmological studies by Kazin et al. (2010). There are 66 093 galaxies from that catalogue within 1 arcsec of a *WISE* source. Requiring at least a 5σ detection in each of the four *WISE* bands leaves only 70 sources because of faint W3 and W4 magnitudes. As a result, for LRGs we enforce the 5σ cuts only in the W1 and W2 bands. This yields a sample of 47 989 galaxies, whose W2 – W3 and W3 – W4 colours are, of course, *not reliable*. To emphasize this point, the 10σ limits for the W3 and W4 bands are shown as solid lines in the two corresponding panels in Fig. 4.
- *Stars*: SDSS Data Release 8 contains 119 million unresolved objects within 1 arcsec of a *WISE* source. To ensure high reliability of SDSS star/galaxy separation we limit the sample to $r < 20$. The majority of these stars are on the main sequence, and sample both

³ Available from <http://sdss.physics.nyu.edu/vagc/>

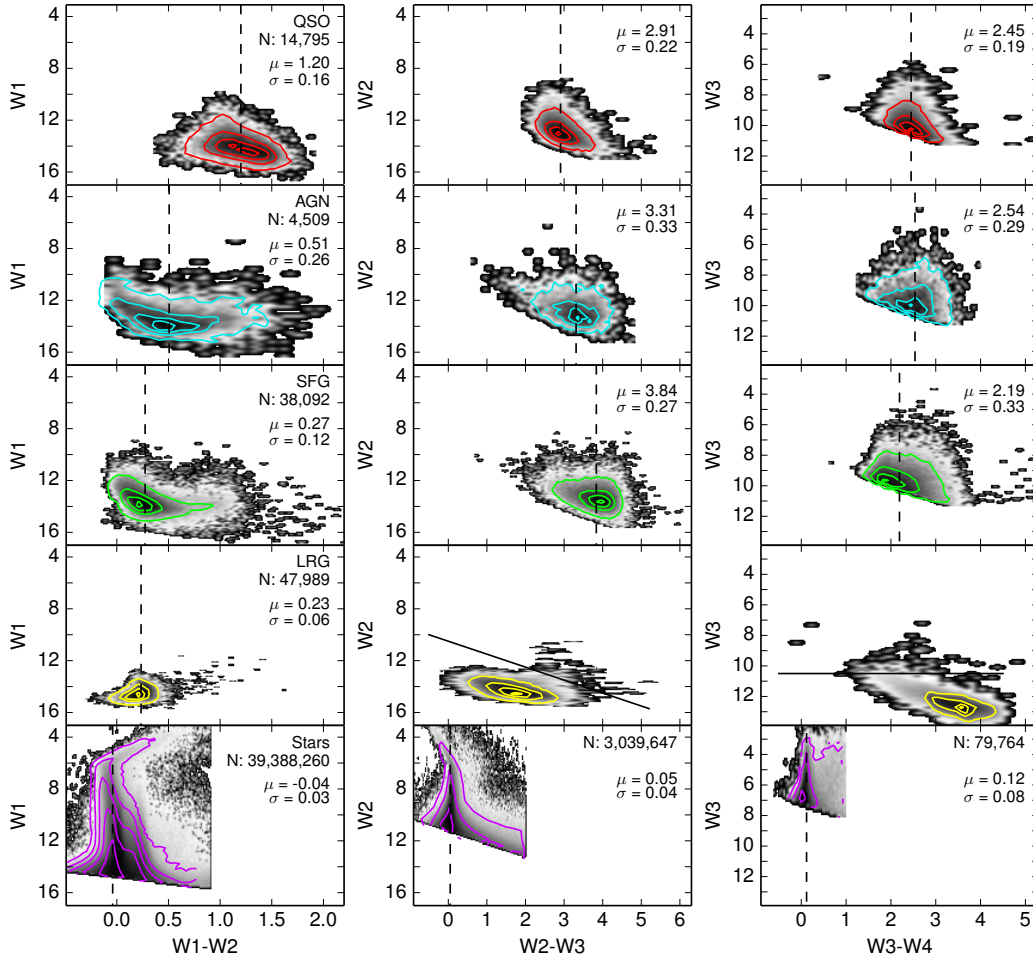


Figure 4. Representative *WISE* CM diagrams for the five major families of objects (rows of panels) classified using SDSS data. The source distribution is rendered using a logarithmic grey-scale map and contours showing 5, 30, 60 and 90 per cent of peak density for each non-stellar sample. For the stars (lower panels), the left sample shows contours at 35, 50, 65, 80 and 95 per cent, the middle one at 55, 75 and 95 per cent, and the right one at 45, 70 and 95 per cent. The number of plotted objects is listed in the top-right corner of each left panel, and it is the same for the entire row unless printed otherwise. The solid lines in the two right-most panels for LRGs show the 10σ limit for the W3 band: the colours of objects with fainter magnitudes are not reliable. Vertical dashed lines in all other panels show median values μ for each distribution, which is indicated together with the corresponding interquartile range σ .

disc and halo populations (see [Ivezić et al. 2012](#), for detailed discussion). Similarly to the case of LRGs, we apply cuts sequentially. We first require $W1 < 15.8$ and $W2 < 14.8$ (10σ limits instead of 5σ because the sample is already fairly large), and $W12 < 0.8$ (to avoid contamination by faint unrecognized quasars; see below), yielding 39 million sources (bottom left panel in Fig. 4). Applying the 10σ cuts also to W3 and W4 bands reduces drastically the sample size, yielding three million sources after the $W3 < 10.5$ cut (bottom centre panel), and $\sim 80\,000$ sources when cuts in all four bands ($W4 < 7.2$) are enforced (bottom right panel).

The final sample sizes for all object classes and their mean *WISE* colours are listed in Table 1. The main conclusion derived from this analysis of SDSS-*WISE* matches is that subsamples of *WISE* sources with $W1 < 11$ must be dominated by Galactic objects, with the increasing fraction of extragalactic objects at fainter magnitudes.

Table 1. Median and interquartile-based standard deviation, $\sigma = 0.74(q_{75} - q_{25})$, of *WISE* colours for the five main source classes. For selection details, see Section 2.

Class	No. selected	W1 – W2	W2 – W3	W3 – W4
QSO ^a	14 795	1.20 ± 0.16	2.91 ± 0.22	2.45 ± 0.19
AGN	4 509	0.51 ± 0.26	3.31 ± 0.33	2.54 ± 0.29
SF	38 092	0.27 ± 0.12	3.84 ± 0.27	2.19 ± 0.33
LRG	47 989	0.23 ± 0.06	n/a	n/a
Stars	79 764	-0.04 ± 0.03	0.05 ± 0.04	0.12 ± 0.08

^aWithout *K*-correction (see [Nikutta et al., in preparation](#)).

2.1 Quasar contamination of the faint stellar sample

For faint ‘stars’, we required $W12 < 0.8$ because *WISE* sources with $W1 \gtrsim 14$ and $W12 > 0.8$ seem to be dominated by quasars that were too faint to be listed in the SDSS quasar catalogue. Strong

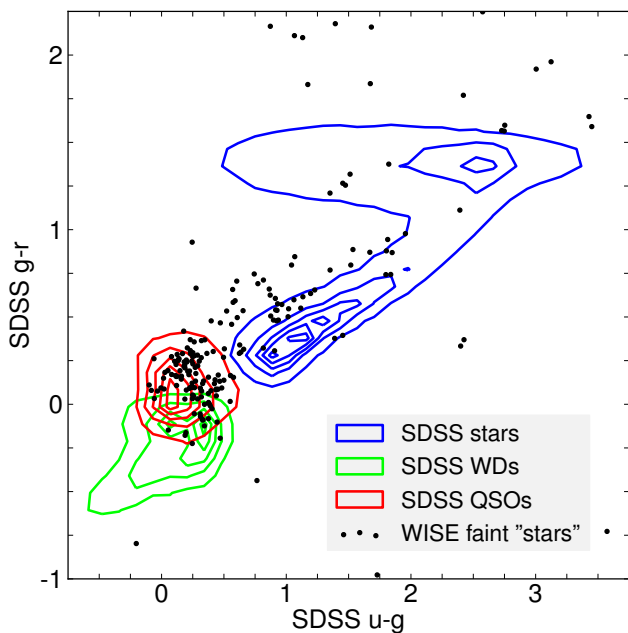


Figure 5. Faint *WISE* sources in SDSS $g-r$ versus $u-g$ CC diagram. Objects that have $WISE\ W1 - W2 > 0.8$ and $W1 \leq 14$ but are unresolved in SDSS imaging are shown as dots. The distributions of true SDSS stars, white dwarfs, and quasars, are shown with contours, as indicated in the legend. All contour levels are 0.1–0.9 in steps of 0.2. Most of the faint *WISE* objects are consistent with quasars that were too faint to be listed in the SDSS quasar catalogue.

support for this hypothesis is provided by their distribution in the SDSS $g-r$ versus $u-g$ CC diagram shown in Fig. 5. Objects that are unresolved in SDSS imaging data and which have $WISE\ W1 - W2 > 0.8$ and $W1 \leq 14$ are shown as dots. All other selection criteria for stars as defined in Fig. 4 were also applied. The distributions of true SDSS stars, white dwarfs, and quasars, are shown as blue, green, and red contours, respectively. We separated the WDs from the SDSS stellar catalogue (940 objects out of a total of $> 430k$) according to fig. 23 in Ivezić et al. (2007), requiring that $u-g < 0.5$ and $g-r < 0$.

Most of our faint *WISE* objects (218 in total, although only 190 dots are visible within the limits of the figure) are found in the region occupied by quasars (see, e.g., fig. 1 in Smolčić et al. 2004). A smaller fraction is further consistent with anomalously red quasars, found along and just above the stellar locus (for details, see Richards et al. 2003). Finally, only very few of the faint objects could be misclassified WDs. White dwarfs, although of similar SDSS $u-g$ colour as QSOs, tend to be significantly bluer in SDSS $g-r$.

3 COLOUR DISTRIBUTION OF BRIGHT OBJECTS

The analysis of SDSS-*WISE* matches shows that *WISE* sources with $W1 < 11$ must be dominated by Galactic objects. In this section we analyse this bright subset in more detail. We start by excluding objects close to the galactic plane ($|b| < 10^\circ$) due to unknown levels of extinction. We then require that the sources have magnitudes between the 5σ sensitivities and the saturation limits in all four bands. We also ask that the signal-to-noise ratio be greater than 5 in bands W1 and W2, and greater than 10 in bands W3 and W4. Finally, by imposing $W1 < 11$ and $W2 < 10$ we end

up mostly with stars. We produced an all-sky map of the selected $\sim 16\,000$ bright sources by subdividing the sky into small patches of constant area on the sphere, about 13.43 deg^2 , using the HEALPIX tessellation scheme (Górski et al. 2005).⁴ The number of objects in each HEALPIX patch was then counted to construct the logarithmic grey-scale map shown in the leftmost panel (0) of Fig. 6. This map, shown in Mollweide projection with Galactic coordinates, reveals the Galactic bulge and the Magellanic Clouds.

From the four *WISE* fluxes one can produce 12 different colours, but only three of them are independent. We choose W12, W23 and W34 as our three independent *WISE* colours. Their 3D distribution for the bright sources is shown in blue in the middle panel (1) of Fig. 6, with the 2D orthogonal projections shown as black scatter plots on the sides of the cube; these are the corresponding CC planes. These three projections are repeated in Panels 2–4, which show the *WISE* CC diagrams for Galactic sources; if Panels 2 and 4 are folded upwards along their common axes with Panel 3, the cube in Panel 1 is reproduced. We proceed now to discuss the structure evident in the *WISE* colour space.

3.1 Naked stars

The *WISE* magnitudes are normalized to the stellar spectrum of Vega, an A-type star. The colours of most stars should thus cluster around zero in the CC diagrams. Indeed, the highest concentration of objects in Figs. 2 and 6 is found around zero colours. These are ‘naked’ stars, i.e. stars without significant circumstellar IR excess. In the case of *IRAS*, all filters sampled the Rayleigh-Jeans tail of every stellar blackbody (see Fig. 1) so that naked stars corresponded to a single point in all CC diagrams. In contrast, *WISE* bands 1 and 2 cover wavelengths short enough to be close to the peaks of some cool stellar spectra, therefore deviations from the zero-position in the CC diagrams can be expected, primarily for stars significantly cooler than Vega.

Fig. 7 shows the three orthogonal *WISE* colours W12, W23, and W34 for naked stars, described by blackbody emission with a large range of surface temperatures T_s ; AGB stars have $T_s \approx 2500\text{ K}$ (see Sections 3.3 and 4.4), while O-type stars reach upward of $50\,000\text{ K}$. Because Wright et al. (2010) used for Vega a slight modification of a $14\,454\text{ K}$ blackbody (see their equation 2), to take care of instrumental/calibration effects, the colours produced by an unmodified Planck function at that temperature are not precisely 0. At higher temperatures, all *WISE* bands fall in the Rayleigh-Jeans domain and the three colours become constant with a slight ($\sim -0.05\text{ mag}$) deviation from zero. At the cool end the deviations are larger, reaching $\sim +0.4\text{ mag}$ for AGB stars. This is the scatter observed in the stellar blob around the colour origin (0,0,0) in Fig. 6 (Panels 1–4). All deviations larger than this intrinsic scatter must be due to radiation reprocessing by a dusty environment.

3.2 Dusty envelopes

The several plumes and blobs that stand out in the *WISE* colour space away from the origin reflect reprocessing of stellar radiation by surrounding dusty envelopes. Such reprocessing redistributes the energy to longer wavelengths, leading to redder colours. The discernible structure is reminiscent of the clustering in *IRAS*-based

⁴ HEALPIX is available at <http://healpix.sourceforge.net>. We specifically used the PYTHON wrapper HEALPY, available at <https://github.com/healpy/healpy>.

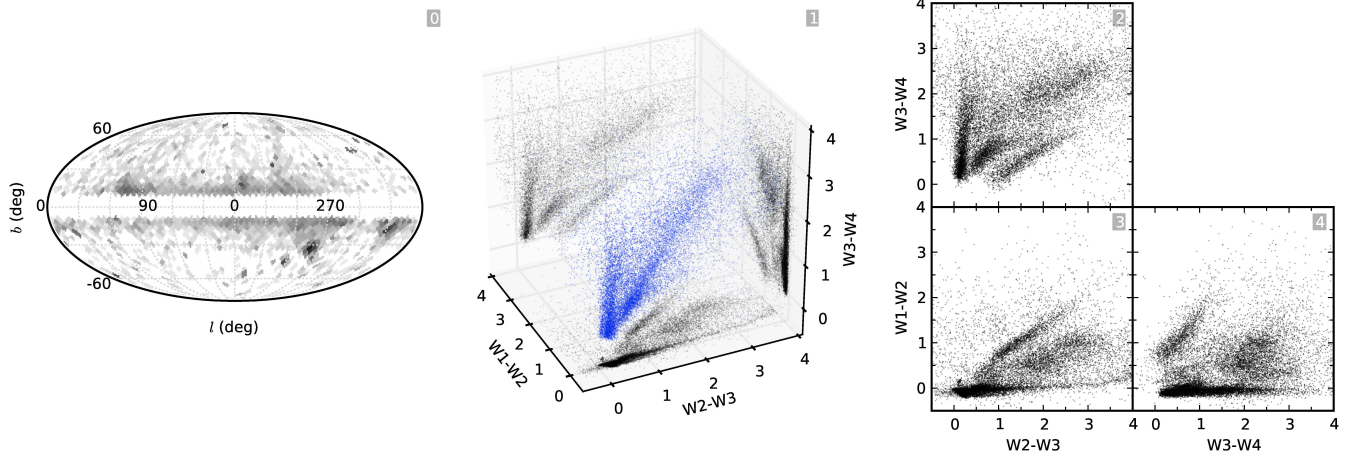


Figure 6. Distribution of 16 000 bright sources with Galactic latitude $|b| > 10^\circ$ on the sky and in *WISE* colour space; see text for all selection criteria. Each panel is numbered in its upper right corner. (0): All-sky map, shown in a Mollweide projection with Galactic coordinates. The logarithmic grey-scale corresponds to the number of sources per unit area in the sky. (1): 3D distribution (shown in blue) of the three independent *WISE* colours W12, W23 and W34. The orthogonal projections on the corresponding CC planes are shown in black scatter diagrams. (2–4): The three *WISE* CC diagrams (sides of the cube in panel 1). Several blobs and plumes are clearly discernible.

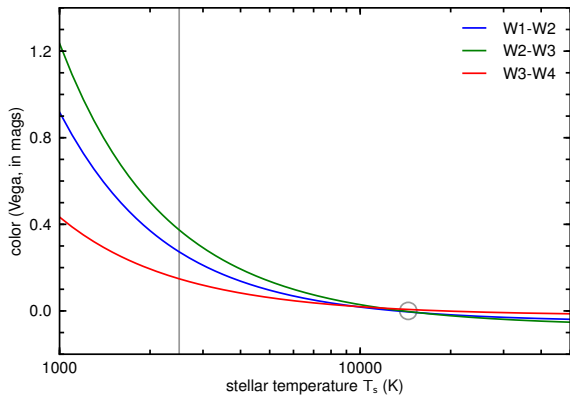


Figure 7. *WISE* colours of ‘naked stars’, represented by blackbody emission with surface temperatures T_s . The grey circle pinpoints the modified-blackbody empirical fit for Vega, adopted by Wright et al. (2010). The grey vertical line at $T_s = 2500$ K marks a typical AGB stellar temperature (see Sections 3.3 and 4.4).

CC diagrams (e.g. van der Veen & Habing 1988; Ivezić & Elitzur 2000). In the case of Galactic *IRAS* sources, these CC structures correspond to different classes of stars. Ivezić & Elitzur (2000) found that they were predominantly young stellar objects (YSO) and AGB stars, and the same is expected for the Galactic *WISE* sources. The narrow, elongated plume parallel to the W23 axis at $W12 \approx 0$ in Panel 3 of Fig. 6 is produced by warm dust emitting predominantly at short IR wavelengths. Such warm emission requires heating by a hot central star and can be expected to be YSO signature. Indeed, Ivezić & Elitzur (2000) found that the locus of *IRAS* colours of YSOs could be reproduced with emission from dust shells with uniform density. Such shells produce the *WISE* colours outlined in Fig. 2 with a red track ($p = 0$), which passes through this plume. Thus this plume is the *WISE* colour locus of YSO sources, which we discuss further in Section 4.3. For now we exclude this plume by retaining only sources with an IR excess in both ‘warm’ colours, $W12 > 0.2$ and $W23 > 0$, concentrating on the other plumes that comprise the AGB sources found by *WISE*.

3.3 AGB stars

The progenitors of asymptotic giant branch (AGB) stars are red giants; their progeny are planetary nebulae and white dwarfs. According to photospheric chemical composition, they can be divided into oxygen-rich (O-rich) and carbon-rich (C-rich) stars. More evolved AGB stars have dusty winds driven by radiation pressure on the dust grains in their circumstellar shells (see e.g.: Elitzur & Ivezić 2001; Ivezić & Elitzur 2010, and references therein). The winds re-process the stellar radiation, shifting the spectral shape towards the infrared. These dusty AGB stars can be divided into two major sub-groups according to dust chemical composition: O-rich stars are associated with silicate-rich dust chemistry and C-rich stars with carbonaceous dust grains.

Dusty AGB stars are observable in our Galaxy and in its close satellites, mostly the Magellanic Clouds, e.g., by *IRAS* (van der Veen & Habing 1988), *ISO* (Trams et al. 1999), *MSX* (Egan et al. 2001), *Akari* (Ita et al. 2008), and *Spitzer* (Vijh et al. 2009; Bolatto et al. 2007) [but see also, e.g., Menzies et al. (2008); Whitlock et al. (2009); Boyer et al. (2013); Dalcanton et al. (2012); Javadi et al. (2013), for other Local Group galaxies]. Studies of the Large Magellanic Cloud (LMC) revealed an overabundance of C-rich objects among its AGB stars, a trend found both at the near-IR wavelengths of the *DENIS* survey (Cioni & Habing 2003, hereafter CH03) and the longer wavelengths of *IRAS* (e.g., Zijlstra et al. 2006). Observations by *IRAS* and 2MASS of AGB stars in our own Galaxy were limited by interstellar dust extinction and by the sensitivities of these surveys (e.g., Jackson et al. 2002, Nikolaev & Weinberg 2000). Thanks to the much improved sensitivity and spatial resolution of *WISE*, the counts of catalogued dusty AGB stars should increase dramatically. This is especially expected for the Galaxy, where a model-based estimate of the total population of dusty AGB stars count is about 200 000 (Jackson et al. 2002).

3.3.1 *WISE*-based selection of dusty AGB stars

To remove the YSOs and still maintain a sizeable sample of AGB sources, first we slightly relaxed the constraint on the Galactic latitudes and omitted all sources with $|b| < 6^\circ$. This excludes most

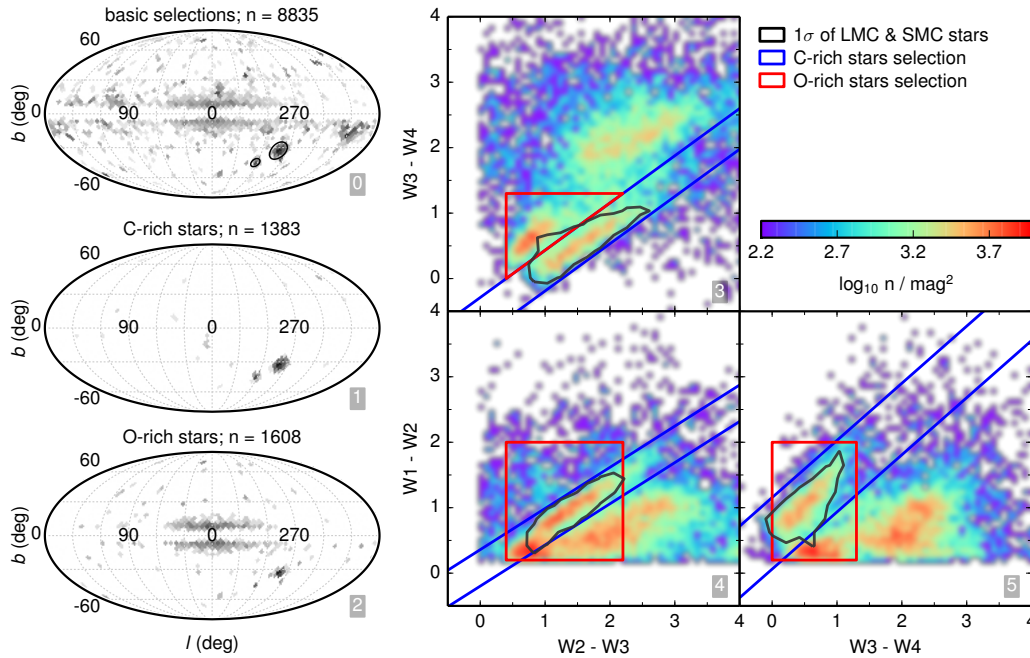


Figure 8. Selection of AGB stars. Each panel is numbered in its lower right corner. (0) All-sky map of bright sources with IR excess in Mollweide projection. The Galactic plane with $|b| < 6^\circ$ has been removed. The grey-scale corresponds to the logarithm of the source count per unit area on the sky. The LMC and SMC are circled in black. (1) Map of C-rich stars selected in the CC diagrams 3–5. This sample is dominated by stars in the Magellanic Clouds. (2) Map of the O-rich stars selected by our criteria. Stars in the Galactic bulge dominate this sample. (3–5) Three *WISE* CC distributions of the sources in Panel 0. The logarithmic colour scale (common to all CC diagrams) shows the number of sources per mag^2 bin. The black contours contain the peak and 68 per cent of all sources within the black circles in Panel 0; these are dominated by the C-rich stars in the LMC. The regions highlighted with blue and red lines delineate our respective selection criteria for C-rich and O-rich stars. The cluster of objects around $W2 - W3 \approx 2$ and $W3 - W4 \approx 2$ contains a mix of Galactic and extragalactic sources, but relatively few AGB stars (see Section 3.3 for details).

YSOs, which cluster around the Galactic plane. We arrived at this choice by testing how well the plumes in Fig. 6 still separate visually when allowing latitudes closer and closer to the Galactic plane. We then removed the narrow, elongated YSO plume as described above (Section 3.2). Finally, we required that the stars must also have colours within boundaries determined from known AGB stars from the SIMBAD data base; a detailed discussion is given in Appendix A. The final sample has 8835 members. Its all-sky distribution is shown in Panel 0 of Fig. 8, where the logarithmic grey-scale corresponds to the normalized number of selected stars per unit area of the sky. Black circles are drawn around the LMC and SMC, with radii of $\sim 8^\circ$ and 4° , respectively.

The colours of AGB sources form a substructure of the 3D blue structure in the *WISE* colour space, shown in Fig. 6. For simplicity, in Fig. 8 we show only the 2D projections of this substructure on the three orthogonal colour planes. Panels 3–5 of this figure show how the selected stars distribute in *WISE* CC diagrams. The black contours contain 68 per cent of all the stars within the two black circles drawn around the LMC and SMC in Panel 0, as well as the peaks of their CC distributions. Since dusty AGB stars in the Magellanic Clouds are dominated by C-rich stars, the plumes outlined with these black contours mark the locus of C-rich stars in the *WISE* colour space. To quantitatively improve the selection of C-rich stars, we define two slab-shaped regions shown with blue lines in Panels 3 and 4; the corresponding blue lines in Panel 5 are a consequence of these definitions. In the 3D colour space, the intersections of these slabs define a parallelepiped within which the selected C-rich stars fall. The centre line of this elongated volume

follows roughly the greatest density of the C-rich star plume (see Appendix A for the mathematical details).

Two structures remain. From cross-checks with SIMBAD, the plume outlined with red is dominated by O-rich AGB stars. The separation between the O-rich and C-rich plumes is cleanest in the $W23-W34$ diagram (Panel 3), where the red triangle is the locus of O-rich AGB stars. The slanted edge of our selection aligns with the C-rich star selection boundary. The edge in $W34$ is tuned to exclude additional objects (dominated by quasars, see below). The $W23$ edge is positioned to maximize the completeness of our O-rich star selection without significant overlap with stars which have very little IR excess, i.e. which might not be AGB stars with circumstellar dust shells. In the two other panels (4 and 5) the separation is not as clean, thus we use for selection criteria the simple rectangular areas outlined in red.

The other structure, around $W12 \approx 0.5$, $W23 \approx 2.7$, and $W34 \approx 2.2$, is disconnected from the origin of the *WISE* colour space. Its objects are a mix of Galactic and extragalactic sources outside the selection boundaries for O-rich and C-rich stars. Cross-checks with SIMBAD show that the blue end of this plume in Panel 3 comprises purely Galactic sources, mostly YSO, variable stars, emission-line stars and only < 10 per cent AGB candidates. The YSOs most likely contribute to the $W3$ band through their polycyclic aromatic hydrocarbon (PAH) emission. Thanks to its especially broad filter ($\sim 7-18 \mu\text{m}$; see Fig. 1), *WISE* band 3 covers the prominent PAH features at 7.7 , 8.6 , and $11.3 \mu\text{m}$, indicative of star formation (e.g. Peeters et al. 2004). Such non-thermal, fluorescent emission is outside the scope of our study. Towards the red end of this plume we find increasingly more and more extragalactic sources (red QSOs,

Seyferts, etc.) that have slipped through our selections. Thus this plume is a diverse mix of objects and will be ignored hereafter.

To summarize, we have demonstrated in this section that it is possible to use *WISE* photometry to select fairly clean samples of O-rich and C-rich AGB stars. We note that our results for the distribution of C-rich stars differ significantly from those in a recent study by [Tu & Wang \(2013\)](#). We believe that their results were affected by saturation effects in *WISE* photometry, as discussed in detail in Appendix A.

3.3.2 Near-IR colours of *WISE*-selected AGB stars

The *WISE*-based selection of AGB stars described in the preceding section is sensitive to the presence of circumstellar dust emission. The success of this selection, as well as the ability of *WISE* colours to distinguish envelopes with carbonaceous dust from those with silicate dust, can be verified using near-IR photometry. Based on published work (e.g., with 2MASS and *DENIS* surveys; [Nikolaev & Weinberg 2000, CH03](#)), AGB stars with carbonaceous dust are expected to be redder than $J - K_s \sim 2$, while stars with silicate dust, and early AGB stars without much dust, have bluer $J - K_s$ colours.

Fig. 9 shows the K_s versus $J - K_s$ CM diagrams constructed with 2MASS photometry for three subsamples of *WISE*-selected AGB stars. These subsamples are selected positionally from low and high Galactic latitudes, and from the LMC region. The expected difference in the $J - K_s$ colour distributions between *WISE*-selected subsamples of stars with carbonaceous and silicate dust is easily discernible. Nevertheless, when the numbers of the two populations are very different (LMC is dominated by C stars and the Galaxy by O stars, see below), the smaller population can be significantly dominated by the larger one.

The *WISE*-selected AGB stars are biased in favour of dusty AGB stars, while samples selected using near-IR photometry (and sometimes visual photometry) are strongly biased against dusty AGB stars. For example, the well-studied sample selected using visual and near-IR photometry from [Cioni \(2009\)](#) does not include any stars with $J - K_s > 2.3$! This selection is controlled by direct photospheric emission while *WISE* fluxes are dominated by re-radiation from dusty shells. These different selection criteria make data analysis and interpretation more difficult, but they are also advantageous because of implicit constraints on age and metallicity distributions of the underlying populations, as we discuss below.

3.3.3 The spatial variation of the C:O star count ratio

With the colour-selection criteria for C-rich and O-rich AGB stars established, Panels 1 and 2 of Fig. 8 show the distributions of these two families in the sky. The C-rich star sample is dominated by stars from the Magellanic Clouds, while O-rich stars are found predominantly towards the Galactic bulge and plane. This behaviour of dusty AGB stars is also seen for samples selected using near-IR photometry (recall that the latter are biased in favour of early AGB stars without thick dusty envelopes): while the Galaxy has more O-rich stars, the LMC and SMC are dominated by C-rich stars ([CH03](#)). This difference is likely due to higher metallicity in the Galactic disc than in LMC/SMC ([Battinelli & Demers 2011](#)).

The all-sky coverage and large size of the *WISE* sample of AGB stars allow us to compute a projected map of the C-to-O-rich star number ratio as a function of sky coordinates. The left panel of Fig. 10 shows in a colour map the variation of this ratio in the Galaxy and its immediate vicinity. The sky was divided into small

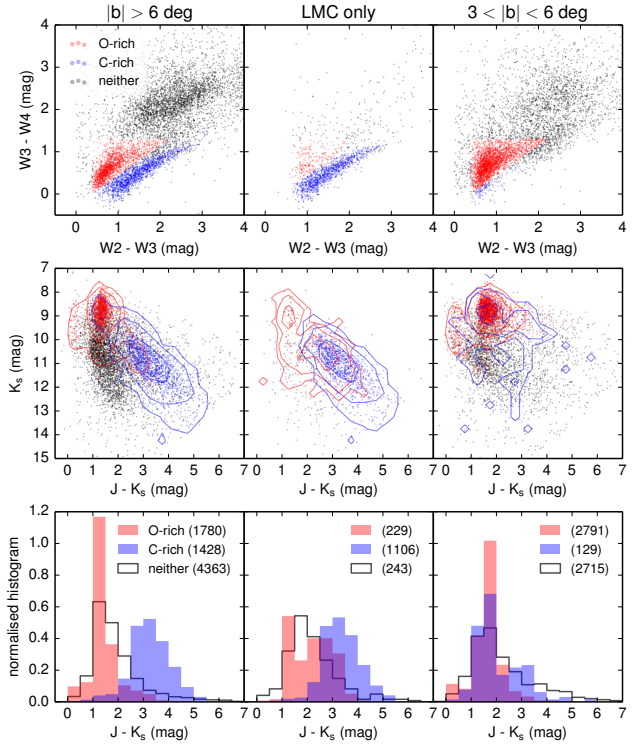


Figure 9. Analysis of near-IR J-K colour distribution for *WISE*-selected stars with circumstellar dust shells. The colour and magnitude selection criteria are as in Fig. 10, but additionally the selected stars must have valid measurements in 2MASS. The three columns correspond to three different positionally-selected subsamples, as indicated at the top. The majority of C-rich stars are found in the LMC, and most have $J - K_s > 2$, consistent with previous work and with models. O-rich stars with silicate dust shells predominantly have $J - K_s < 2$. The O-rich sample from the LMC (middle column) and the C-rich sample from low Galactic latitudes (right column) appear contaminated by much more numerous samples of C-rich and O-rich stars, respectively.

13.43 deg² patches (see Section 3), and the ratio was determined per patch. For this map we have dropped the previous requirement to exclude objects close to the Galactic plane, and selected all stars based on the colour and magnitude criteria defined previously. A strong gradient in the ratio, from the lowest values in the Galactic plane to the highest C-rich star concentration in the Magellanic Clouds, is clearly visible. The dynamical range spans almost four orders of magnitude.

Several regions stand out and are marked with (projected) circles: the Galactic Centre, and the LMC and SMC. Quite surprisingly, the Sagittarius Dwarf Spherical Galaxy (Sgr DSph) is also clearly discernible. The coordinates of these four regions are taken from the NASA/IPAC Extragalactic Database (NED) and are listed in Table 2 (lines 1 and 2). For the outlined circles we adopted radii 1.5 times the reported optical semi-major axes (line 3). For the Galactic Centre region we chose a radius identical to the LMC.

The right panel of Fig. 10 shows histograms of the C:O ratio for each sub-region, measured among all non-empty patches in that region. The histograms were obtained using the “Bayesian Blocks” technique devised by [Scargle et al. \(2013\)](#). This method maximizes Bayesian evidence for a model under the assumption that data can be described by a piece-wise step function with arbitrarily located knots (analogous to a histogram with variable bin width). We used the implementation provided in the

`plotting.hist_tools.bayesian_blocks` function from the `ASTROML` package (Vanderplas et al. 2012; Ivezić et al. 2014). The C:O-rich star ratio for Sgr DSph is about 1.5 orders of magnitude higher than in the Galactic plane, though less than that of the Magellanic Clouds. Table 2 lists the means (line 8) and ranges (lines 9 & 10) of the histograms in Fig. 10, together with the values measured for the full sky. Line 7 also reports the C:O ratios for the entire sample of stars in each region, without regard for their spatial distribution within that region. In the LMC, this value deviates significantly from the mean of all small in-region patches (line 8).⁵ The conclusion is that the C:O ratio in the LMC is not spatially uniform.

3.3.4 The C:O star count ratio in LMC

To investigate the spatial variation of the C:O ratio in LMC, we analyse it as a function of radial distance from the LMC centre. We apply the coordinate transformations laid out in a two-paper series on the structure of the Magellanic Clouds, van der Marel & Cioni (2001) and van der Marel (2001) (hereafter MC1 and MC2). These transformations de-project the disc of the LMC to a face-on view and thus enable the measurement of the C:O ratio in concentric rings around the LMC centre. See Appendix B for the exact procedure. Fig. 11 shows in its left top panel the stars in the LMC in equatorial coordinates. The samples after de-projecting and applying our *WISE* colour and magnitude selection criteria for C-rich and O-rich AGB stars are shown in the left bottom panel. C-rich stars are shown in blue ($n_C = 1114$), O-rich in red ($n_O = 238$), and other stars as black dots ($n = 330$). The two grey rings are at 5 and 10 kpc radial distance from the LMC centre, and in the LMC disc. The two distributions of radial distances are indeed different. A two-sided Kolmogorov–Smirnov test of the two samples yields a p -value $\approx 6.5 \times 10^{-6}$, allowing us to reject the hypothesis that both are drawn from the same underlying distribution at a highly significant level. In fact, if we knew that both samples were distributed normally, with their respective means and variances, this p -value would afford rejection with $\sqrt{2} \operatorname{erf}^{-1}(1 - p) = 4.5\sigma$ confidence.

To test for the existence of a radial gradient in the C:O ratio, we construct empirical cumulative distribution functions (CDF) of the radial distances of the C-rich and O-rich stars from the LMC centre. The CDFs are shown as blue and red lines in the right top panel of Fig. 11, and are defined as $\operatorname{CDF}(d) = \sum_{i=1}^n 1_{\{d_i < d\}}$. This function increases by one at each observed distance d_i in the sorted list of distances, i.e. it counts the number of stars observed up to a distance d . A proper CDF would need to be normalized by $1/n$, but we refrained from doing so in the right top panel, to show how the absolute member counts in the two samples differ. To obtain analytic representations of the CDFs we fitted them with polynomials of various degrees, and also with the CDFs of Normal distributions. The best fits could be obtained with fourth degree polynomials, which were significantly better than third degree polynomials and Gaussians. The fitted polynomial function is $P_4 \equiv \sum_{i=0}^4 a_i x^i$, with coefficients $a_i = (-76.37, 256.03, 6.38, -4.54, 0.26)$ for the CDF of C-rich stars, and $a_i = (-30.77, 107.91, -15.00, 0.65, 0.01)$ for O-rich stars (lowest order first). The fits are plotted with dotted lines in the top right panel of Fig. 11.

The second panel from the top on the right shows the fractional residuals of our fits (their absolute values). They are gener-

ally well-controlled at a level <5 per cent, except in the innermost region. The third panel from the top shows as red and blue lines the probability density functions (PDF) of the two samples, obtained as derivatives $\partial \operatorname{CDF} / \partial d$ of the fitted CDFs and normalized to unit area. Also shown are histograms of the distributions of radial distances, which were obtained using Bayesian Blocks. The striking similarity of the PDFs obtained by polynomial fits of the empirical CDFs, and the histograms computed *independently* via Bayesian Blocks, demonstrates that the results are not strongly affected by methodology. Encouraged by this agreement, we plot in the right bottom panel of Fig. 11 the ratio of the (unnormalised) PDFs of the C-rich and O-rich AGB samples, i.e. the radial C:O number count ratio in the LMC. The value increases from ~ 3 in the innermost regions to $\lesssim 19$ at about 6 kpc, before turning down sharply. This downturn is probably not reliable because the number counts of both C-rich and O-rich stars are quite small at these distances. In fact, Feast et al. (2010), who re-analysed the *DENIS* data of Cioni (2009) by removing unpopulated areas in the LMC sky, find a similar trend in the C:O star count ratio (C:M star ratio, to be more precise), and furthermore derive large uncertainties for the data points beyond ~ 7 kpc (see their fig. 6).

It is reassuring that both the Feast et al. (2010) results and our analysis show the same trend of increasing C:O ratio with distance from the LMC centre. Nevertheless, there are significant differences. Between 2 and 6 kpc from the centre, the region where the results of both studies can be considered reliable, Feast et al. find a variation from approximately 0.25 to 0.5 while we find much larger ratios that range from ~ 4 to 18, a larger dynamic range as well. As discussed above, the two determinations of the C:O ratio involve different properties. The Cioni sample used by Feast et al. was selected from the photospheric emission of AGB stars while our *WISE* selected samples are based on the radiation from the dusty shells that typify late stages of evolution of these stars. That a much larger C:O ratio is determined from dust re-radiation than from photospheric emission implies a higher efficiency of dust formation for the C-rich stars. A detailed comparison of the two results or, equivalently, predicting the variation of the C:O ratio for dusty AGB stars from the variation observed for early AGB stars, would require detailed modelling of AGB evolution (e.g., Marigo et al. 2008; Girardi et al. 2010). In addition to prescriptions for AGB evolution of both O-rich and C-rich stars, their age and metallicity distributions and the dust formation efficiency also need to be known or assumed. While such an effort is beyond the scope of this study, it has the potential to shed new light on the formation and evolution of the LMC.

4 MODELLING WISE COLOURS

Why do objects segregate in colour space and what causes the particular segregation patterns of different families of *WISE* sources? These questions were already addressed by Ivezić & Elitzur (2000) in the context of *IRAS* sources. The dust radiative transfer problem possesses general scaling properties, as discussed in detail by Ivezić & Elitzur (1997). There are only two input quantities whose magnitudes matter: the dust optical depth at some fiducial wavelength and its temperature at some position in the source. All other input is defined by dimensionless, normalized profiles that describe (1) the spectral shapes of the dust absorption and scattering coefficients, (2) the spectral shape of the external heating radiation, and (3) the dust spatial distribution. Physical dimensions, e.g. luminosity and linear sizes, are irrelevant. Scaling applies to arbitrary geometries

⁵ A similar deviation is seen in Sgr DSph, but the number of contributing patches might be too small for meaningful conclusions.

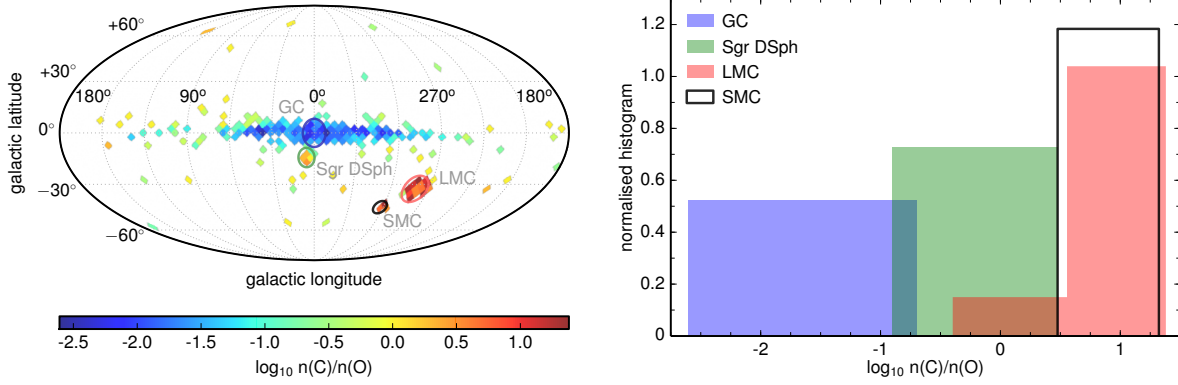


Figure 10. Left: all-sky map of the local C-to-O-rich star number ratio, in Mollweide projection. The Galactic Centre is at (0,0). This map is a ratio of Panels 1 and 2 in Fig. 8, but without the $|b| > 6^\circ$ criterion. The colour scale shows the logarithm of the ratio per 13.43 deg^2 coordinate bin (defined by the HEALPIX tessellation). The locations of the Galactic Centre and three Milky Way satellites are indicated with (projected) circles. Right: Distribution of $\log_{10} n(\text{C})/n(\text{O})$ in each circular area from the left panel. The histograms were obtained using Bayesian Blocks (see text). See Table 2 for statistics.

Table 2. Number ratio of C-to-O AGB stars in the Galactic vicinity. The circular regions selected in Fig. 10 and their properties are listed in lines 1–10. Valid patches are those that contain both C-rich and O-rich stars.

No.	Quantity	Full sky	GC	Sgr DSph	SMC	LMC
1	Galactic longitude (deg)	n/a	0.	5.57	302.80	280.47
2	Galactic latitude (deg)	n/a	0.	-14.17	-44.30	-32.89
3	Radius (deg)	n/a	8.06	5.62	4.00	8.06
4	Number of C-rich stars $n(\text{C})$	1629	60	21	161	1079
5	Number of O-rich stars $n(\text{O})$	14 969	4500	62	24	235
6	Number of valid HEALPIX patches	196	21	7	3	14
	$\log_{10} n(\text{C})/n(\text{O})$					
7	For entire selection	-0.96	-1.88	-0.47	0.83	0.66
8	Mean of valid patches	-0.85	-1.71	-0.19	0.84	0.87
9	Min of valid patches	-2.61	-2.61	-0.90	0.48	-0.40
10	Max of valid patches	1.38	-0.70	0.48	1.32	1.38

and implies that *different dusty objects are expected to segregate in CC diagrams primarily because their dust shells are different, not because they have different central sources*. This behaviour is displayed by the objects in the *IRAS* PSC and is similarly expected for *WISE* colours.

We now describe our basic modelling framework for dusty stellar environments and then discuss comparisons of models with data in more detail. All modelling was performed with our public code *DUSTY* (Ivezić et al. 1999).

4.1 Model properties

We employ two families of dust grains. Our ‘standard ISM’ dust contains a standard Galactic mix of 53 per cent silicates, with optical constants from the Ossenkopf et al. (1992) ‘cold dust’ for silicate, and 47 per cent graphite, with optical properties from Draine (2003). The other family represents pure-composition dust typically found in AGB stars. Dust around C-rich stars comprises amorphous carbon, whose properties we take from Hanner (1988), while for O-rich stars we take the warm silicates from Ossenkopf et al. (1992). We assumed spherical grains and considered both single-size dust grains and models with MRN grain-size distribution (Mathis, Rumpl, & Nordsieck 1977). *DUSTY* handles dust dis-

tributions through the composite grain approximation by averaging over the chemical composition and size distribution. This approach was shown to reproduce reasonably accurately the results from exact treatment of grain mixtures (see e.g. Efstathiou & Rowan-Robinson 1994). The extinction profiles used in the calculations are shown in Fig. 12.

With *DUSTY* we produced models of spherical dust shells around central sources; the code calculates exact solutions for the dust temperature profiles, emerging flux and other properties of interest. As noted above, the only input parameters whose magnitudes matter are the dust temperature on the shell inner boundary and the shell overall optical depth at a given wavelength; all other model input describes dimensionless, normalized profiles. We computed a range of dusty shell models with overall optical depth at visual from $\tau_V = 0.1$ to 200 and dust temperature on the inner boundary from $T_d = 300$ K to 1200 K. The spectral shape of the central source was taken as a blackbody with temperature $T_s = 2500$ K, 5000 K and 10 000 K. For the radial density distribution of the spherical dusty shell we used a power-law r^{-p} with $p = 0, 1$ and 2. In addition, for the AGB shells we used the radial density profiles determined from a solution of the full equation of motion of radiatively driven dusty winds, obtained with the RDW option of *DUSTY* (see Elitzur & Ivezić 2001). The shell relative thickness, ra-

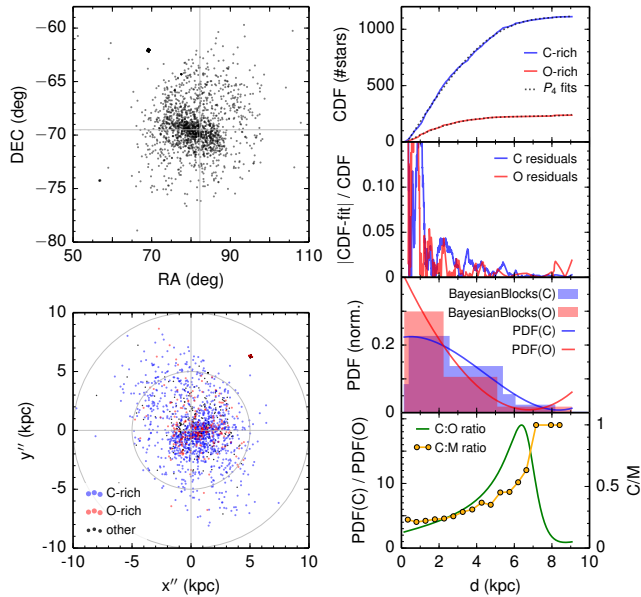


Figure 11. C:O number ratio gradient in the LMC. Left top: stars in the LMC in equatorial coordinates. Left bottom: de-projected map of the LMC, following MC1 and MC2 (see text, and Appendix B). C-rich AGB stars are shown in blue, O-rich in red, and others in black. The axes indicate linear distances (in kpc) in the disc plane of the LMC. The two circles are at 5 and 10 kpc from the adopted LMC centre. Right top: empirical CDF of the C-rich and O-rich distributions of radial distances from the LMC centre. Shown as dotted lines are polynomials of fourth degree, fitted to the observed CDFs. Right, second from top: fractional residuals $|\text{CDF-fit}|/\text{CDF}$. Right, third from top: the derivatives $\partial\text{CDF}/\partial d$ of the fitted polynomials, i.e. the PDF of the distributions of radial distances from the LMC centre, up to 10 kpc. The PDFs are normalized to unit area. Also shown are normalized histograms of the radial distances, obtained using the *Bayesian Blocks* method, which guarantees optimal binning. Right bottom: C:O ratio (green) as a function of radial distance d . It was obtained by dividing the two (un-normalized) PDFs from the panel above, and uses the left vertical axis. The C:M count ratio found by Feast et al. (2010, see their fig. 6) is shown in orange, and uses the right vertical axis. Both vertical axes span the range from 0 to $1.1 \times$ the maximum of the C:O or C:M curves, respectively. The curves are reliable only up to distances of ~ 6 kpc, beyond which the uncertainties are very large due to small source number counts per radial annulus. See Section 3.3.4 for details.

ratio of outer to inner radius $Y \equiv R_{\text{out}}/R_{\text{in}}$, was taken as 100. Resulting SEDs for some representative cases are shown in Fig. 13.

4.2 Colour tracks

As noted above (Section 3.1), a naked star corresponds to a point near the origin of the *WISE* colour space. Surrounding the star with a dust shell will shift the colours to the red, moving the source away from the origin. Given the shell properties and varying only its overall optical depth, the dust temperature profile remains unchanged as long as the shell remains optically thin. Therefore the colours remain the same; all optically thin dusty shells with the same properties correspond to a single point in the colour space. Increasing the optical depth further, the shell temperature profile starts to change when it enters the optically thick regime, leading to deviation of the source colours away from the optically-thin point towards redder colours. This results in a track in the 3D *WISE* colour space, with position along the track determined by the shell overall optical depth τ_V . Projections on the 2D colour planes pro-

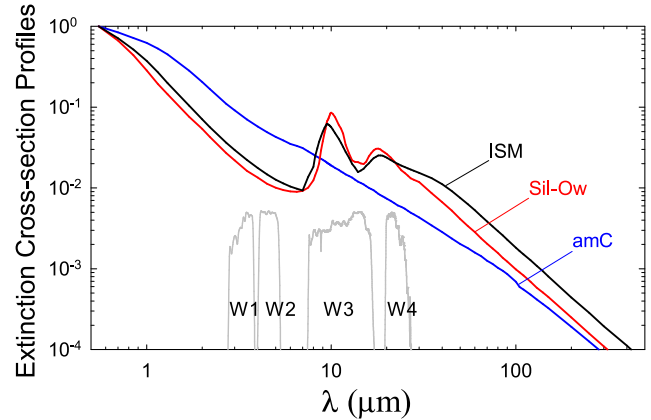


Figure 12. Extinction cross-sections, normalized to unity at $0.55 \mu\text{m}$, of model dust for spherical grains with an MRN size distribution. Black: standard ISM dust mixture from Ossenkopf et al. (1992) and Draine (2003). Red: warm silicates from Ossenkopf et al. (1992) (Oss-w). Blue: amorphous carbon from Hanner (1988) (amC). The shapes of the *WISE* filter response functions are outlined in light grey.

duce tracks in CC diagrams, like those shown in the right panel of Fig. 2. This figure shows that the tracks for $p = 0$ and 1 shells of ISM dust trace the boundaries of the region occupied by extragalactic sources in the W12–W23 CC diagram. This behaviour is in agreement with the findings by Levenson et al. (2007) and Sirocky et al. (2008) that the deep silicate absorption features observed in ULIRG spectra require burial of luminous central sources in very optically thick ($\tau_V \gtrsim 100$) dusty shells with flat ($p = 0$ –1) radial density distributions. The figure also shows that stars occupy a region much closer to the colour origin so that the optical thicknesses of their dust shells are generally much smaller.

We now discuss in detail the *WISE* colours of Galactic sources. Tabulations of the colour tracks used in figures displayed below are provided in Table C1, where we also list the model in-band fluxes, useful for studies which depend on source luminosity.

4.3 YSO tracks

Ivezić & Elitzur (2000) found that *IRAS* colours of YSOs could be explained by the colour tracks of dust shells with flat ($p = 0$) density distributions. Fig. 14 explores in detail the *WISE* colours expected from $p = 0$ and 1 radial profiles for spherical shells of ISM dust with MRN size distribution and optical depths up to $\tau_V = 30$, heated by a central 10 000 K blackbody. Models were produced for dust temperatures on the shell inner boundary varying from $T_d = 300$ K to $T_d = 1200$ K. This figure provides a zoom-in on the smaller- τ_V region of the tracks for shallow density distributions that were shown in Fig. 2. Its various plots show the range of possibilities for colour tracks covering the likely region of parameter space for dust shells around YSOs. A characteristic feature of flat density distributions is that even a small increase in optical depth can significantly enhance long wavelength emission because it places more dust at large radial distances with low temperatures. For this reason, the $\tau_V < 1$ portions of the tracks are parallel to the colour axis with longer wavelengths while maintaining a value of roughly 0 for the other axis with the ‘warmer’ colour. Deviations from this behaviour increase with T_d and are mostly noticeable in the W23–W34 diagram, especially for the $p = 1$ tracks.

Fig. 15 shows the comparison with observations. Its three pan-

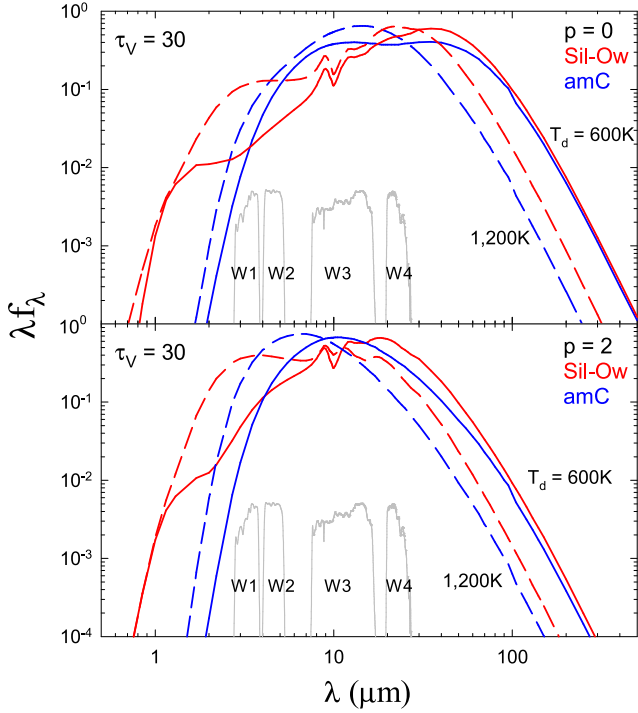


Figure 13. Model SEDs for spherical dust shells, centrally heated by a 10 000 K source. Silicate dust models are shown in red, amorphous carbon in blue. In both cases the grains follow the MRN size distribution and the extinction profiles are shown in Fig. 12. The shell optical depth is $\tau_V = 30$ at visual, its relative thickness is $Y = 100$ and its temperature on the inner boundary is either $T_d = 600$ K (solid lines) or $T_d = 1200$ K (dashed). The density profiles are power-law r^{-p} with $p = 0$ and 2, as marked. The shapes of the *WISE* filter response functions are outlined in light grey.

els reproduce the projections on to 2D colour planes of the 3D colour distribution of bright *WISE* sources that were shown previously in Fig. 6, with model tracks plotted over the source distribution. The models producing these tracks are the same as the $p = 0$ models shown in Fig. 14 except for the spectral shape of the heating source: instead of a pure blackbody they use the empirical Vega fit employed for normalization by Wright et al. (2010) (see also Section 3.1). These tracks follow rather well the long, narrow plume of stars along the W23 and W34 axes at $W12 \approx 0$ in Panels 1 and 2 of Fig. 15 and along the W34 axis at $W23 \approx 0$ in Panel 0. This plume has been previously identified as the locus of YSOs among bright *WISE* sources (Section 3.2). In most colour-colour combinations, little differentiates the tracks for different values of T_d , the dust temperature on the inner boundary. The tracks diverge significantly only in the panels involving the W34 colour combination, where only the $T_d = 1200$ K track passes through the blobs roughly clustered around (2.5, 2) in Panel 0 and (2.2, 0.7) in Panel 2. It is not clear, though, that these blobs give a reliable indication of thermal dust emission because these sources could be dominated by PAH emission covered by the broad W3 filter (see Section 3.3). A reliable determination of the nature of these sources would require in-depth, detailed modelling of individual objects.

The small range of optical depths spanned by the main plume of SF sources implies that *WISE* has uncovered a large number of YSO with small amounts of dust around them while giving little indication of such objects covered by deep layers of dust. This is surprising because heavy dust obscuration is expected in many YSOs. Indeed, the SF regions identified by *IRAS* were characterized by

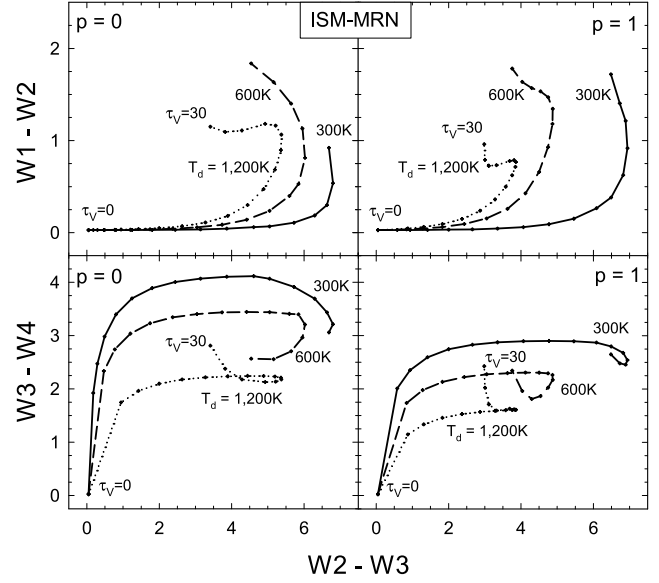


Figure 14. Model colour tracks for spherical dusty shells around a central blackbody source with $T_s = 10\,000$ K. The shell density profile is a power-law r^{-p} with $p = 0, 1$, as marked. Each track starts at the colours of the dust-free blackbody and the optical depth increases along the track from $\tau_V = 0$ to $\tau_V = 30$. The dust is taken as ISM type with MRN size distribution. In each panel different tracks correspond to dust temperature T_d on the shell inner boundary of 300 K (solid lines), 600 K (dashed lines) and 1200 K (dotted lines).

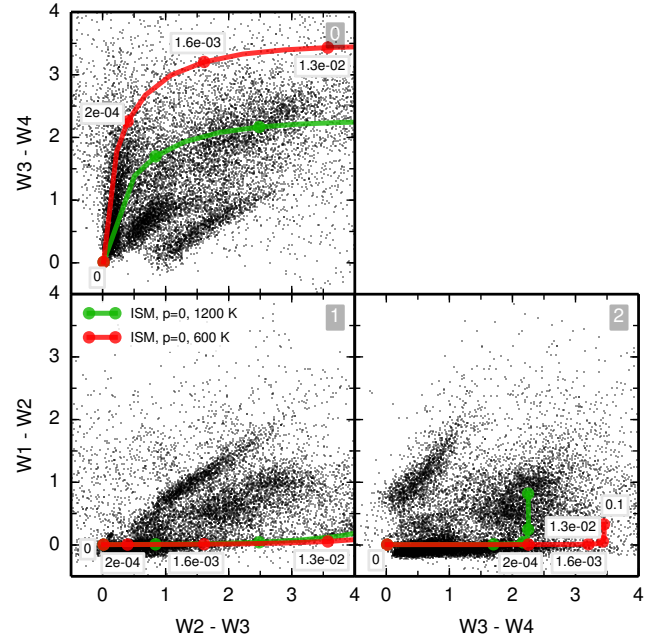


Figure 15. Colour distributions of Galactic sources, as in Fig. 6; each panel is numbered at its top right corner. Overplotted are model colour tracks of spherical dusty shells with standard ISM dust grains and uniform density profiles ($p = 0$). The shells surround central stars with Vega-like emission. The dust temperature on the shell inner boundary is either 600 K (red tracks) or 1200 K (green). Position along the track depends only on the dust optical depth; a few values of the *V*-band optical depth are marked. The tracks delineate the plume of YSOs.

large optical depths ($\tau_V \sim 1\text{--}10$; see fig. 3 in Ivezić & Elitzur 2000). These differences reflect the starkly different sensitivity limits of the two facilities. *IRAS* required for detection strong IR emission, which precluded sources with optically thin dusty shells. However, optically thick YSO shells, which were a prerequisite for *IRAS* detection, produce *WISE* colour differences that exceed 4. Such large differentials are eliminated by the cuts we place on saturation limits, which remove sources too bright at short wavelengths, and on signal-to-noise ratio, which remove sources too weak at the long wavelength bands. As is evident from Fig. 2, the W23 colour of optically thick $p = 0$ objects is larger than 4, entering the domain populated by extragalactic sources which we deliberately sought to avoid in this analysis. Relaxing our selection criteria should therefore reveal a heavily obscured YSO population mixed with the extragalactic sources.

To test this hypothesis we identified in our basic selections those sources that are moderately bright in W1 and are matched by high optical depths of our model colour tracks. These would most likely be YSOs with high shell optical depths. Such a population, compatible with the previous *IRAS* detections, indeed exists in the *WISE* data base. It can be found approximately within $10 \leq W1 \leq 11$, $0.4 \leq W12 \leq 1.4$, and $4 \leq W23 \leq 5.7$. All sources with $10 \leq W1 \leq 11$ are shown in the CC scatter diagram in Fig. 16 (left panel); all other selection criteria from Fig. 15 apply, except that the constraint on Galactic latitude was dropped. The CC diagram contains 29 892 sources while the blob outlined with a blue rectangle contains 6192 objects, presumably YSOs with high dust optical depths. Indeed, the centre of the selection cube, $W1 = 10.5$, $W12 = 0.9$, $W23 = 4.85$, implies that $W3 = 4.75$ (Vega). With this magnitude we can use $F_\nu = F_\nu^{\text{iso}} \times 10^{-m_{\text{Vega}}/2.5}$ to compute the in-band flux density F_ν , where F_ν^{iso} is the zero-magnitude flux density in Jansky. It is given as 31.674 Jy for band 3 in Jarrett et al. (2011, see their table 1). Thus our W3 magnitude $m_{\text{Vega}} = 4.75$ corresponds to ≈ 0.4 Jy at $12 \mu\text{m}$ (W3) while the faint limit of the *IRAS* Faint Source Catalogue at $12 \mu\text{m}$ is 0.2 Jy. Therefore, our findings are compatible with *IRAS* discovering only sources in the blue box but not those with lower $12 \mu\text{m}$ fluxes. Also plotted in the left panel of Fig. 16 are the same model colour tracks from Panel 1 of Fig. 15, but over an expanded colour range. The green track ($T_d = 1200$ K) shows a turn-over at $W23 \sim 5.5$, and all its τ_V values between 0.025 and 9.4 stay perfectly within the blue YSO rectangle. The right panel of Fig. 16 shows the all-sky distribution of the ~ 6200 sources from the YSO plume. The distribution is extremely heavily concentrated towards the Galactic plane, a preferred location to find local SF regions. This is further evidence that our conclusions are consistent. The choice of dusty shell models for YSOs can be debated because some young stars, e.g. T Tauri stars, are known to be surrounded by dusty disks. Vinković et al. (2003) showed that a flared disk produces an SED identical to that of an equivalent optically thin spherical dust shell. The latter is thus a good proxy for the more realistic disk model. There is no way to distinguish between them, or any combination of the two, with flux measurements alone; imaging is necessary for that. From equations 7 and 8 in section 2.1 of Vinković et al., a constant density shell (as applied in our YSO models) is equivalent to a disk with linear flaring. The very small optical depths we find in the *WISE* data of YSOs may be also interpreted as the difference in flaring angle across the disk (Equation 7), but it is difficult to decide without imaging.

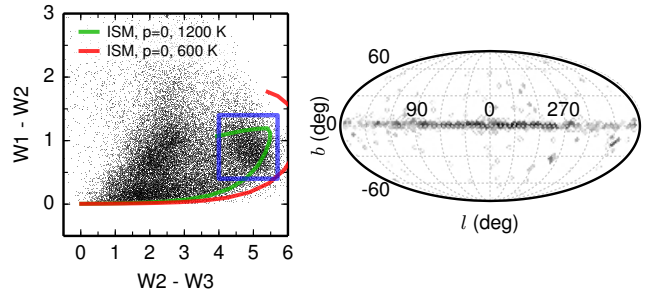


Figure 16. Identifying YSOs in the *WISE* data base. Left: distribution of all sources with $10 \leq W1 \leq 11$ in a *WISE* CC diagram. All other cuts are as in Fig. 15, except that there is no constraint on Galactic latitude. The green and red *DUSTY* model colour tracks are as in Fig. 15. The blue rectangle outlines the expected colour region of YSOs with high dust obscuration. Right: all-sky distribution of the sources in the blue rectangle (in Mollweide projection), with the grey-scale normalized to peak source count density. It is heavily concentrated towards the Galactic plane, where local SF regions are predominantly found.

4.4 AGB tracks and model parameter constraints

Radiatively driven winds (RDW) have been shown to well describe infrared emission from dusty envelopes around AGB stars (see, e.g.: Elitzur & Ivezić 2001; Ivezić & Elitzur 2010, and references therein). Their circumstellar dust distribution approximately follows a power-law $1/r^2$. *DUSTY* can calculate RDW models exactly and in Fig. 17 we show RDW model colour tracks for a central source at $T_s = 2500$ K and a $Y = 100$ shell. Tracks are shown for two temperatures at the inner dust boundary, $T_d = 600$ K and $T_d = 1200$ K. AGB stars are classified as O-rich or C-rich stars (see Section 3.3) and models were produced with two corresponding types of dust: warm silicates from Ossenkopf et al. (1992) (Sil-Ow, left panels), and amorphous carbon (amC, right panels). Both single-size grains and an MRN size distribution were used, as indicated in the legend. As seen from Fig. 17, the effect of different grain sizes on the colour tracks is negligible compared to varying the dust temperature.

Amorphous carbon absorbs more in the W1 and W2 bands, while silicates absorb more in the W3 and W4 bands (see Fig. 12). Therefore, given two circumstellar shells with the same overall optical depth but different chemical composition, the silicate shell is expected to be redder in the $W2 - W3$ colour and bluer in the $W1 - W2$ colour. As illustrated in Fig. 17, the *WISE* colour diagrams can separate sources with steep density profile and predominantly silicate dust (e.g. typical AGB stars) from those with carbonaceous dust (e.g. carbon stars), for the same dust sublimation temperature.

How do the RDW model tracks compare to AGB colours measured by *WISE*? First, we can fix the stellar temperature T_s at 2500 K and the ratio of inner-to-outer radius of the shells at 100, since both are quite typical values for AGB stars. We also investigated other T_s , but they did not agree as well with the data (the allowed temperature range is only a few hundred K wide). The two most important free model parameters are dust interface temperature, T_d , and shell optical depth, τ_V . This two-dimensional space of model parameters maps to *WISE* colour space (and vice versa).

We have demonstrated in Section 3.3 that AGB stars can be selected using only *WISE* photometry. Equations (A3)–(A8) in Appendix A are the mathematical definitions of our selection criteria. The corresponding loci of AGB stars are visualized in Fig. 8 with red and blue lines. These equations also define lower and upper

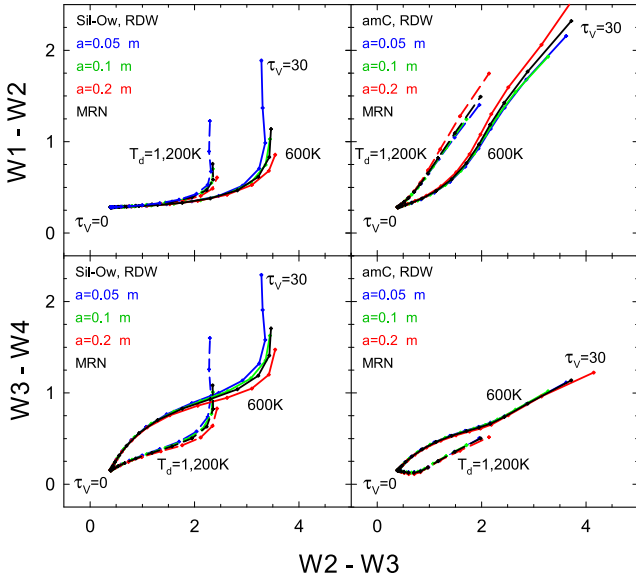


Figure 17. Model colour tracks for dusty RDW around a central star with $T_s = 2500$ K. Left panels are for silicate dust (Sil-Ow), right panels – for amorphous carbon (amC). The dust temperature T_d at the wind origin is taken as 600 K (solid lines) and 1200 K (dashed lines). Model tracks for various grain sizes and for the MRN size distribution are colour coded as marked. The overall optical depth of the shell increases along each track from $\tau_V = 0$ to $\tau_V = 30$.

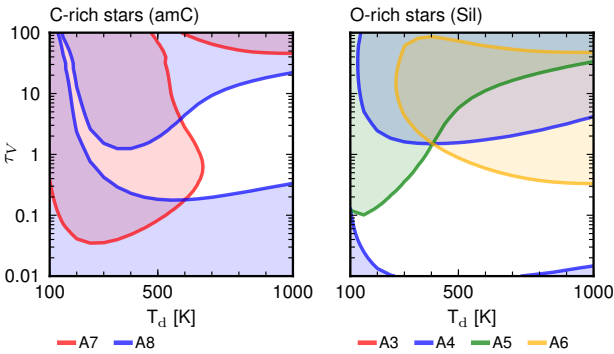


Figure 18. Translation of our AGB colour selection criteria [defined in equations (A3)–(A8)] into model parameter constraints. Left for C-rich AGB stars, right for O-rich stars. Each equation translates into curved areas in the (T_d, τ_V) parameter space. The excluded areas are shaded (see legend for the colour/equation code). Only the white fraction of each panel contains permissible model parameter combinations. See text for details.

bounds of several *WISE* linear colour combinations. For instance, equation (A7) can be written as $x - 0.629y \in [-0.198, 0.359]$ (where $x = W1 - W2$, $y = W2 - W3$). With given dust properties (for example, amorphous carbon dust), we can compute the value of this linear colour combination, $x - 0.629y$, for any *DUSTY* model parameter combination (T_d, τ_V) . Then the colour selection criterion demands that this value be within $[-0.198, 0.359]$. Therefore, the interval boundaries are simply contours in the parameter plane, and are plotted as solid lines in Fig. 18 (for amorphous carbon dust in the left panel, for O-rich star models in the right panel). The legends relate the equation numbers to colours used for plotting. The areas outside of the interval are excluded by the selection criterion, and are shown shaded in the figure. Each of the colour-selection equations (A3)–(A8) translates to such parameter-exclusion areas.

The complement of their union is the only portion of the parameter space with permissible combinations. It is shown in white in Fig. 18.

Since our C-rich star colour selection volume is confined quite tightly (cf. Fig. 8), the allowed parameter space for *DUSTY* models is also well-constrained. The dust shells must have interface temperatures not lower than ≈ 600 K and the visual optical depths are in the range $\approx 0.2 - 20$. For O-rich star models the selection in CC space was not as tight; consequently the permissible parameter ranges are less well-constrained. Our results seem to indicate that C-rich AGB stars tend to have higher maximal optical depths than O-rich AGBs, and that they lack the very lowest τ_V values. In contrast, O-rich AGB models extend to smaller optical depths, and values larger than a few are excluded. This conclusion is supported by samples analysed in Ivezic & Elitzur (2010); see their figs 5 and 6, with data from Young (1995), Richards & Yates (1998) and Olofsson et al. (1993) (we caution the reader that those data sets may be affected by unknown selection effects). We emphasize that our results should be viewed qualitatively and note that the parameter boundaries are ‘soft’ because they depend on the exact colour selection criteria.

The distribution of C-rich and O-rich AGB stars in the *WISE* colour space, as previously selected in Section 3.3 and Appendix A, is shown in Fig. 19. Overplotted are fiducial RDW model colour tracks, for which the temperature at the inner boundary is $T_d = 800$ K (solid lines) or $T_d = 500$ K (dotted), in accordance with the parameter ranges found above. All tracks are computed for a shell thickness of 100, and with a stellar temperature of $T_s = 2500$ K, as explained before. Panels 00–02 (left side) show our C-rich star selection and colour tracks computed with amorphous carbon dust, while Panels 10–12 (right) show our O-rich star selection and tracks with ‘warm’ circumstellar silicates from Ossenkopf et al. (1992). The model tracks do not match all AGB plumes in all three orthogonal projections simultaneously, but the range spanned by models of these dust interface temperatures brackets well the observed *WISE* colours of AGB stars.

The $T_d = 800$ K RDW model with amorphous carbon dust (blue solid line) follows the plume of C-rich stars reasonably well in all three two-dimensional projections of the *WISE* colour space (Panels 00–02). Although the agreement is not perfect, it is likely that these 0.2–0.3 mag large offsets could be rectified with minor modifications of the dust opacity. We have not attempted a detailed study because such small changes could also be explained by deviations from spherical symmetry, non-uniform dust distribution, variations in photospheric temperature as the star ascends the asymptotic giant branch sequence, and possibly other effects. These degeneracies cannot be broken with only three *WISE* colours. The red tracks in Panels 10–12 of Fig. 19 correspond to a fiducial model for O-rich stars with standard silicate dust opacity and $T_d = 800$ K and 500 K. Models in this temperature range bracket the 3D distribution of O-rich AGBs in the *WISE* colour volume. It is remarkable that most of the extension of this O-rich star plume can be covered with shell optical depths below a value of unity.

5 SUMMARY AND DISCUSSION

With detections for about 560 million objects, *WISE* represents a major step forward in the surveying and understanding of the infrared sky. Its combination of up to 1000 times higher sensitivity than previous IR surveys, and a relatively high angular resolution, enables studies of source samples with unprecedented statistical

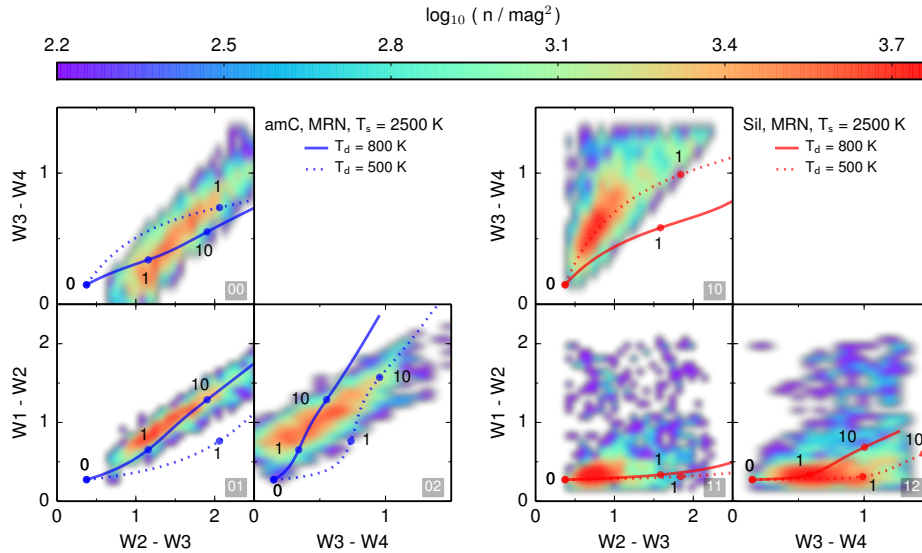


Figure 19. Colours of AGB stars measured by *WISE*, and fiducial *DUSTY* model colour tracks for RDW. The number distribution of observed AGB colours is shown with a logarithmic colour scale for C-rich (left panels) and O-rich AGB stars (right panels). Overplotted as solid and dotted lines are fiducial *DUSTY* model colour tracks computed for both chemistries, with two dust interface temperatures that bracket the observed colours (see legend). The total radial optical depth of the shell models is printed at some positions along the tracks.

significance. We have computed colour tracks in the *WISE* photometric system for two families of models: smooth spherical shells and clumpy dust torus models, and decided to study local/Galactic populations in this paper, and the extragalactic sky in Nikutta et al. (in preparation).

The model tracks provide guidance for the observed distribution of sources in *WISE* CC diagrams, such as illustrated in the left panel in Fig. 2. The main results of our computations are shown in the right panel in Fig. 2. The model-based colour tracks outline reasonably well the distribution of sources expected to be associated with dust emission (i.e. all source types except T dwarfs and stars without dusty shell). The location of dust-free stars coincides very well with the optically thin point of all dust-shell models irrespective of the dust composition. Deviations from the zero-point are caused by *WISE* filters W1 and W2 being sensitive to the blackbody peaks of the coolest stars, thus producing colours other than those for the Rayleigh–Jeans slope. In the other extreme, at high optical depths, the *DUSTY* model tracks of ISM dust shells with shallow radial density distributions overlap with those CC areas populated by Ultra-Luminous Infrared Galaxies (ULIRGs), which are known to be deeply shrouded in dust (Sirocky et al. 2008).

We find that *WISE* photometry alone is sufficient to reliably classify C-rich and O-rich asymptotic giant branch stars with dusty shells (Section 3.3). With the large population of AGB stars in the *WISE* Catalogue we were able to define magnitude and colour selection criteria that distinguish between the two classes. It is necessary to regard the distribution of *WISE* colours as a three-dimensional arrangement in colour–colour–colour space. The traditional two-dimensional orthogonal projections are very helpful, but not sufficient. With the ability to cleanly separate the local populations of C-rich and O-rich AGB stars we computed the most detailed map of the C:O-rich star count ratio for the Milky Way and its satellites (see Section 3.3.3). We find a strong spatial gradient away from the Galactic plane, with the Magellanic Clouds showing a C:O ratio about 1000 times higher than the Galactic bulge. We also clearly uncover the Sagittarius Dwarf Spheroidal Galaxy

in the map. We find that the C:O dusty AGB star ratio increases with distance from the LMC centre about twice as fast as measured for near-IR selected samples of early AGB stars. Detailed modelling of these measurements has the potential to shed new light on the formation and evolution of LMC.

DUSTY model tracks for shells with RDWs follow the identified AGB plumes well. By mapping the previously found colour selection criteria to model parameters, specifically inner dust shell temperature T_d and shell optical depth τ_v , we found observational constraints on these model parameters. They seem to indicate slight differences in the physical properties of C-rich and O-rich AGB shells (see Section 4.4).

Spherical dusty shell models with flat radial density distributions generate *WISE* colours compatible with YSOs. YSO samples selected using *IRAS* and *WISE* surveys have very little overlap due to vastly different imaging depths: while *IRAS* was sensitive to bright sources with relatively high visual optical depths, *WISE* detects much fainter YSOs with relatively small optical depths (see Section 4.3).

To investigate further how well models describe the *WISE* colours of IR sources, sufficiently large samples need to be studied object-by-object, with SED fitting for each source over a large wavelength range. The *Spitzer* SAGE Survey (Meixner et al. 2006), for instance, has been previously used for such a task. Riebel et al. (2012) matched the IR *Spitzer* spectra with optical and near-IR data to produce broad-band SEDs for more than 30 000 AGB stars in the LMC, and fitted them with *GRAMS* models (Sargent et al. 2011; Srinivasan et al. 2011). Thanks to *WISE*, a similar study can be now undertaken for AGB stars in the Galaxy.

CLUMPY models of AGN dust torus emission, with their more complicated geometry and dust distributions, are much better than simple spherical shells in explaining the general location of QSOs and other AGNs in the *WISE* CC diagram. The location of the highest CLUMPY model density aligns almost perfectly with the centre of the circular region identified as ‘Seyferts’ by Wright et al. in the left

panel of Fig. 2. A detailed study of the *WISE* colours of AGNs will be presented in the companion paper (Nikutta et al., in preparation).

Acknowledgements: We are grateful to Maria-Rosa Cioni for illuminating discussions and for making her data available to us. We reproduced fig. 12 from Wright et al. (2010) as part of our Fig. 2 by permission of the AAS and the authors. We thank Chao-Wei Tsai for providing us a high-quality version. We thank both referees for their helpful suggestions which improved the paper. We express our gratitude to Xavier Koenig for reminding us of the disk/shell dichotomy of YSO models (see Section 4.3), and to James Davenport for his insightful post-submission comments on the variability information in the *WISE* database. We are also thankful to Patricia Arévalo and Ron Wilhelm for helpful discussions. RN acknowledges support by the ALMA-CONICYT fund, project No. 31110001, and by FONDECYT grant No. 3140436. ŽI thanks the Hungarian Academy of Sciences for its support through the Distinguished Guest Professor grant No. E-1109/6/2012. ŽI and NHW acknowledge support by NSF grant AST-1008784 to the University of Washington. ME acknowledges NASA support and the award of an NPP Senior Fellowship from ORAU, which supported a sabbatical leave at JPL/Caltech where much of this work was completed. This publication makes use of data products from the Wide-field Infrared Survey Explorer, which is a joint project of the University of California, Los Angeles, and the Jet Propulsion Laboratory/California Institute of Technology, funded by the National Aeronautics and Space Administration. Funding for SDSS-III has been provided by the Alfred P. Sloan Foundation, the Participating Institutions, the National Science Foundation, and the U.S. Department of Energy Office of Science. The SDSS-III web site is <http://www.sdss3.org/>. SDSS-III is managed by the Astrophysical Research Consortium for the Participating Institutions of the SDSS-III Collaboration including the University of Arizona, the Brazilian Participation Group, Brookhaven National Laboratory, Carnegie Mellon University, University of Florida, the French Participation Group, the German Participation Group, Harvard University, the Instituto de Astrofísica de Canarias, the Michigan State/Notre Dame/JINA Participation Group, Johns Hopkins University, Lawrence Berkeley National Laboratory, Max Planck Institute for Astrophysics, Max Planck Institute for Extraterrestrial Physics, New Mexico State University, New York University, Ohio State University, Pennsylvania State University, University of Portsmouth, Princeton University, the Spanish Participation Group, University of Tokyo, University of Utah, Vanderbilt University, University of Virginia, University of Washington, and Yale University. This research has made use of the NED which is operated by the Jet Propulsion Laboratory, California Institute of Technology, under contract with the National Aeronautics and Space Administration. Some of the results in this paper have been derived using the HEALPIX/HEALPY package (Górski et al. 2005).

REFERENCES

- Baldwin, J. A., Phillips, M. M., & Terlevich, R. 1981, *PASP*, 93, 5
- Battinelli, P., & Demers, S. 2011, in *ASP Conf. Ser.*, Vol. 445, *Why Galaxies Care about AGB Stars II: Shining Examples and Common Inhabitants*, ed. F. Kerschbaum, T. Lebzelter, & R. F. Wing, 479
- Blanton, M. R., et al. 2005, *AJ*, 129, 2562
- Bolatto, A. D., et al. 2007, *ApJ*, 655, 212
- Boyer, M. L., et al. 2013, *ApJ*, 774, 83
- Cioni, M.-R. L. 2009, *A&A*, 506, 1137
- Cioni, M.-R. L., & Habing, H. J. 2003, *A&A*, (CH03), 402, 133
- Covey, K. R., et al. 2007, *AJ*, 134, 2398
- Dalcanton, J. J., et al. 2012, *ApJS*, 198, 6
- Draine, B. T. 2003, *ApJ*, 598, 1017
- Efstathiou, A., & Rowan-Robinson, M. 1994, *MNRAS*, 266, 212
- Egan, M. P., Van Dyk, S. D., & Price, S. D. 2001, *AJ*, 122, 1844
- Elitzur, M., & Ivezić, Ž. 2001, *MNRAS*, 327, 403
- Feast, M. W., Abedigamba, O. P., & Whitelock, P. A. 2010, *MNRAS*, 408, L76
- Girardi, L., et al. 2010, *ApJ*, 724, 1030
- Górski, K. M., Hivon, E., Banday, A. J., Wandelt, B. D., Hansen, F. K., Reinecke, M., & Bartelmann, M. 2005, *ApJ*, 622, 759
- Hanner, M. 1988, *Grain optical properties*, Technical report
- Ita, Y., et al. 2008, *PASJ*, 60, 435
- Ivezić, Ž., Beers, T. C., & Jurić, M. 2012, *ARA&A*, 50, 251
- Ivezić, Ž., Connolly, A., Vanderplas, J., & Gray, A. 2014, *Statistics, Data Mining and Machine Learning in Astronomy* (Princeton University Press)
- Ivezić, Ž., & Elitzur, M. 1997, *MNRAS*, 287, 799
- Ivezić, Ž., & Elitzur, M. 2000, *ApJ*, 534, L93
- Ivezić, Ž., & Elitzur, M. 2010, *MNRAS*, 404, 1415
- Ivezić, Ž., Nenkova, M., & Elitzur, M. 1999, *arXiv:astro-ph/9910475*
- Ivezić, Ž., et al. 2007, *AJ*, 134, 973
- Jackson, T., Ivezić, Ž., & Knapp, G. R. 2002, *MNRAS*, 337, 749
- Jarrett, T. H., et al. 2011, *ApJ*, 735, 112
- Javadi, A., van Loon, J. T., Khosroshahi, H., & Mirtorabi, M. T. 2013, *MNRAS*, 432, 2824
- Kazin, E. A., et al. 2010, *ApJ*, 710, 1444
- Levenson, N. A., Sirocky, M. M., Hao, L., Spoon, H. W. W., Marshall, J. A., Elitzur, M., & Houck, J. R. 2007, *ApJ*, 654, L45
- Marigo, P., Girardi, L., Bressan, A., Groenewegen, M. A. T., Silva, L., & Granato, G. L. 2008, *A&A*, 482, 883
- Mathis, J. S., Rumpl, W., & Nordsieck, K. H. 1977, *ApJ*, 217, 425
- Meixner, M., et al. 2006, *AJ*, 132, 2268
- Menzies, J., Feast, M., Whitelock, P., Olivier, E., Matsunaga, N., & da Costa, G. 2008, *MNRAS*, 385, 1045
- Nenkova, M., Sirocky, M. M., Ivezić, Ž., & Elitzur, M. 2008a, *ApJ*, 685, 147
- Nenkova, M., Sirocky, M. M., Nikutta, R., Ivezić, Ž., & Elitzur, M. 2008b, *ApJ*, 685, 160
- Neugebauer, G., et al. 1984, *ApJ*, 278, L1
- Nikolaev, S., & Weinberg, M. D. 2000, *ApJ*, 542, 804
- Nikutta, R., Hunt-Walker, N., Nenkova, M., Ivezić, Ž., & Elitzur, M. 2013, *MNRAS*, to be submitted (paper II)
- Obrić, M., et al. 2006, *MNRAS*, 370, 1677
- Olon, F. M., et al. 1986, *A&AS*, 65, 607
- Olofsson, H., Eriksson, K., Gustafsson, B., & Carlstrom, U. 1993, *ApJS*, 87, 305
- Ossenkopf, V., Henning, T., & Mathis, J. S. 1992, *A&A*, 261, 567
- Peeters, E., Spoon, H. W. W., & Tielens, A. G. G. M. 2004, *ApJ*, 613, 986
- Richards, A. M. S., & Yates, J. A. 1998, *Irish Astronomical Journal*, 25, 7
- Richards, G. T., et al. 2003, *AJ*, 126, 1131
- Riebel, D., Srinivasan, S., Sargent, B., & Meixner, M. 2012, *ApJ*, 753, 71
- Sargent, B. A., Srinivasan, S., & Meixner, M. 2011, *ApJ*, 728, 93
- Scargle, J. D., Norris, J. P., Jackson, B., & Chiang, J. 2013, *ApJ*, 764, 167

Schneider, D. P., et al. 2010, *AJ*, 139, 2360
 Sirocky, M. M., Levenson, N. A., Elitzur, M., Spoon, H. W. W., & Armus, L. 2008, *ApJ*, 678, 729
 Smolčić, V., et al. 2004, *ApJ*, 615, L141
 Soifer, B. T., Neugebauer, G., & Houck, J. R. 1987, *ARA&A*, 25, 187
 Srinivasan, S., Sargent, B. A., & Meixner, M. 2011, *A&A*, 532, A54
 Trams, N. R., et al. 1999, *A&A*, 346, 843
 Tu, X., & Wang, Z.-X. 2013, *Research in Astronomy and Astrophysics*, 13, 323
 van der Marel, R. P. 2001, *AJ*, (MC2), 122, 1827
 van der Marel, R. P., & Cioni, M.-R. L. 2001, *AJ*, (MC1), 122, 1807
 van der Veen, W. E. C. J., & Habing, H. J. 1988, *A&A*, 194, 125
 Vanderplas, J., Connolly, A., Ivezić, Ž., & Gray, A. 2012, in *Conference on Intelligent Data Understanding (CIDU)*, 47
 Vjih, U. P., et al. 2009, *AJ*, 137, 3139
 Vinković, D., Ivezić, Ž., Miroshnichenko, A. S., & Elitzur, M. 2003, *MNRAS*, 346, 1151
 Whitelock, P. A., Menzies, J. W., Feast, M. W., Matsunaga, N., Tanabé, T., & Ita, Y. 2009, *MNRAS*, 394, 795
 Wright, E. L., et al. 2010, *AJ*, 140, 1868
 York, D. G., et al. 2000, *AJ*, 120, 1579
 Young, K. 1995, *ApJ*, 445, 872
 Zijlstra, A. A., et al. 2006, *MNRAS*, 370, 1961

APPENDIX A: SELECTION CRITERIA FOR AGB STARS

In order to develop selection criteria for AGB stars, we follow Tu & Wang (2013) and analyse the *WISE* colour distribution of known AGB stars listed in the SIMBAD data base. Aided by their results, our procedure is simpler. They first selected about 76 million sources from the full *WISE* All-Sky source catalogue with detections in W1, W2 and W3 bands (and free of contamination and confusion flags in all four bands) that have a unique 2MASS source within 3 arcsec. Then they positionally matched this sample to objects listed in the SIMBAD data base within 2 arcsec (except in the case of high proper-motion stars which were matched within 4 arcsec), and further restricted the sample to 20 degrees from the Galactic plane, yielding a sample of 3.2 million sources. This sample includes AGB stars, as well as all other sources known to SIMBAD and detected by *WISE*, which satisfy the selection criteria.

We begin by obtaining a sample of stars from SIMBAD whose main identifier was consistent with AGB stars (AGB star, C star, S star, OH/IR star, or Mira-type variable), resulting in 32 556 objects. The positions of these stars were matched to the positions of objects in the *WISE* All-Sky source catalogue within 2 arcsec, rejecting sources with more than one association. The resulting sample of 24 942 stars is further reduced by rejecting all sources with contamination and confusion flags, as well as removing sources outside of saturation limits (bands W1 through W3) and 5σ faint limits (see Section 1), yielding the final sample of 6171 objects with presumably both reliable *WISE* photometry and reliable SIMBAD classifications.

We did not enforce any cut on Galactic coordinates. The distribution of this sample in representative CC and CM diagrams constructed with 2MASS and *WISE* photometry is shown in Fig. A1. As known from previous work, most AGB stars have 2MASS colour $J - K_s > 1$. Most of them also show clear *WISE* colour excess, $W12 > 0$ and $W23 > 0$, as well as $K_s - W3 > 0$. The

two magnitudes limits discernible from the source distribution in the top right panel are due to adopted faint limit $W3 < 11.32$ and saturation limit $W1 > 8.1$.

The latter is responsible for a significant difference between the data distribution in our $W2 - W3$ versus $W1 - W2$ diagram (the bottom left panel) and the diagram shown in fig. 4 from Tu & Wang (2013). Their version displays C stars below the dashed line in our bottom left panel, and OH/IR stars above the dashed line. Based on this separation, they proposed the dashed line as a separator between these two classes of AGB stars. However, in our version, all the stars below the line are absent, as well as all OH/IR stars, and the region above the line is dominated by C stars, and not by OH/IR stars! It turns out that these differences are caused by rejecting stars brighter than saturation limits - when we relax this criterion, we obtain a data distribution reminiscent of fig. 4 from Tu & Wang (2013). This is shown in Fig. A2, similar to Fig. A1, but now includes formally saturated stars. All saturated stars, with $W1 < 8.1$ and $W2 < 6.7$, are shown with red dots, while the black dots show unsaturated sources. Notice in the lower left panel that almost all saturated stars fall below the dashed line that Tu & Wang (2013) have devised to separate C-rich from O-rich AGB stars. They did not mention saturation limits in their work. We believe that substandard *WISE* photometry for saturated AGB stars has induced unreliable source distribution in fig. 4 from Tu & Wang (2013). The W2 band is most likely to blame, as evidenced by fig. 8 (in section VI.3.c.i.4) of the *WISE* Explanatory Supplement (see footnote 1), where the bias for saturated sources is most pronounced in W2.

With saturation limits enforced, the distribution of C stars, by and large from LMC and SMC, clearly stands out in Fig. A1 (see the bottom right panel). We define the 3D colour space $x = W1 - W2$, $y = W2 - W3$, $z = W3 - W4$. The box that outlines a high concentration of C-rich AGB stars is defined by

$$1.59x - 0.57 < y < 1.59x + 0.32 \quad (\text{A1})$$

$$-0.63x + 1.20 < y < -0.63x + 5.07. \quad (\text{A2})$$

In the $W2 - W3$ versus $W1 - W2$ diagram shown in the bottom left panel of Fig. A1, O-rich stars with silicate dust are seen as a low-density cloud towards the left from the C-rich star box. Further insight in the distribution of O-rich and C-rich AGB stars in *WISE* CC diagrams is based on complete *WISE* samples and is discussed in Section 3.3.

Based on this analysis our samples of AGB stars for Fig. 8 are selected as follows. The initial criteria are:

$W1/W2/W3/W4 < 16.83/15.60/11.32/8.0$	5σ -limits
$W1/W2/W3/W4 > 8.1/6.7/3.8/-0.4$	saturation limits
$W1 < 11, W2 < 10$	only bright sources
$SNR1 \& 2 > 5, SNR3 \& 4 > 10$	signal-to-noise ratio

The regions with $|b| < 6$ deg were also excluded because YSOs tend to cluster in the Galactic plane (Ivezić & Elitzur 2000), and also because of the uncontrolled/unknown levels of Galactic extinction at these latitudes. In the xyz colour space defined above we also require $x > 0.2$, $0 < y < 4$, excluding the long narrow plume of stars with constant-density dust shells. This so-selected initial AGB sample consists of 8835 sources.

To select O-rich AGB stars from this initial sample we used the colour-colour diagrams 3–5 in Fig. 8 as a guideline. We defined

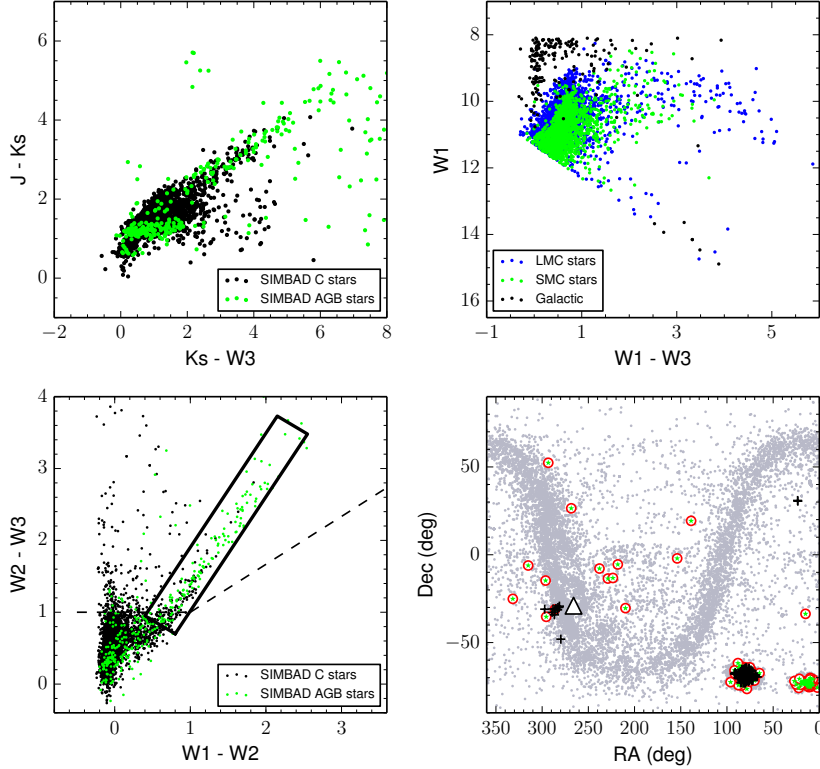


Figure A1. Distribution of *WISE* sources whose classification listed in the SIMBAD data base is consistent with them being AGB stars. Top left panel: the $J - K_s$ versus $K_s - W3$ diagram of *WISE* sources identified in SIMBAD as C stars (black) and AGB stars (green, includes both O-rich and C-rich stars); similar to fig. 1 from Tu & Wang (2013), except that saturated stars are not included, resulting in essentially all OH/IR stars being rejected. Top right panel: the $W1$ versus $W1 - W3$ diagram for all AGB stars in the Galaxy (black), LMC (blue), and SMC (green); similar to fig. 3 from Tu & Wang (2013). Bottom left panel: the $W2 - W3$ versus $W1 - W2$ diagram for C stars (black) and AGB stars (green); similar to fig. 4 from Tu & Wang (2013). The black box outlines a concentration of C-rich AGB stars. The dashed line was proposed by Tu & Wang as a separator between OH/IR and C-rich AGB stars, but see text for our disagreement. Bottom right panel: the sky distribution in equatorial coordinates for stars within the black box in the bottom left panel, using the same colour scheme (green dots are encircled for better visibility). The entire sample of AGB, C, S, OH/IR, and Miras from SIMBAD with *WISE* detection, but without magnitude limits are plotted in the background for reference; the distribution outlines the Galactic disc. The Galactic Centre is marked by the large triangle.

a wedge-shaped volume bounded by these criteria:

$$0.2 < x < 2 \quad (\text{A3})$$

$$0.4 < y < 2.2 \quad (\text{A4})$$

$$0 < z < 1.3 \quad (\text{A5})$$

$$z > 0.722y - 0.289 \quad (\text{A6})$$

The selected O-rich star sample has 1608 members.

The C-rich stars, visible as a strongly elongated plume in Fig. 8, were selected by carving out a 3D elongated volume around the plume. It is the intersection of the following two slabs:

$$0.629y - 0.198 < x < 0.629y + 0.359 \quad (\text{A7})$$

$$0.722y - 0.911 < z < 0.722y - 0.289 \quad (\text{A8})$$

Note that (A7) is the inverse of (A1), and that we abandon (A2). The C-rich star sample contains 1383 sources.

For the C:O-rich star ratio map in Fig. 10 we have relaxed the $|b| < 6$ deg requirement, and have selected C-rich and O-rich star candidates through the CC volumes and magnitudes defined above. The preselected sample contains 90 114 sources, of which 14 969 end up in the O-rich star group. The size of the C-rich star selection grows to 1629 objects.

APPENDIX B: LMC COORDINATE TRANSFORMATIONS

To obtain a de-projected map of the LMC disc, for our analysis of the radial gradient of the C:O-rich star ratio in Section 3.3.3, we follow the procedure outlined in two papers on the structure of the Magellanic Clouds, MC1 and MC2. We begin with the right ascension and declination angles α and δ of our colour and magnitude selected C-rich and O-rich AGB stars (given in degrees or radians). We further assume as the origin of this equatorial coordinate system $(\alpha_0, \delta_0) = (82^\circ.25, -69^\circ.5)$, as defined in Section 4.1 in MC1. This origin corresponds to the centre of the density iso-contours of the *DENIS* survey, but is slightly offset w.r.t. the standard locus of the LMC centre [e.g. $(\alpha_0, \delta_0) = (80^\circ.9, -69^\circ.76)$ given in the NED data base]. From equation (1) of MC1 we obtain the formula for transformed angular coordinate ρ

$$\rho = \arccos \left\{ \cos \delta \cos \delta_0 \cos(\alpha - \alpha_0) + \sin \delta \sin \delta_0 \right\}. \quad (\text{B1})$$

Merging equations 2 and 3 from the same paper we get the other transformed coordinate ϕ

$$\phi = \arctan \left\{ \frac{\sin \delta \cos \delta_0 - \cos \delta \sin \delta_0 \cos(\alpha - \alpha_0)}{-\cos \delta \sin(\alpha - \alpha_0)} \right\}. \quad (\text{B2})$$

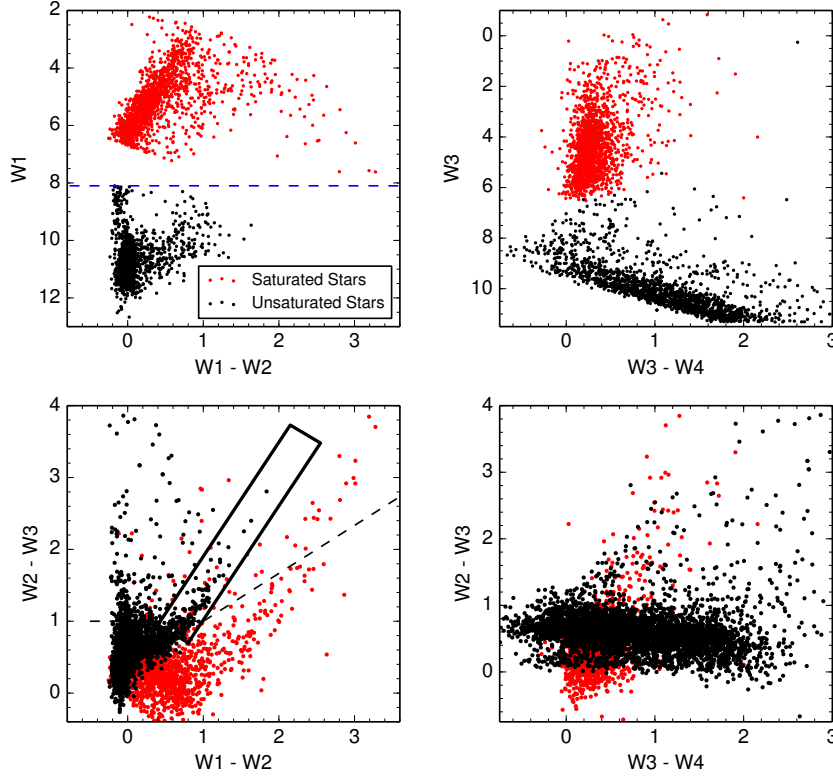


Figure A2. Similar to Fig. A1, but including saturated sources (with $W1 < 8.1$ and $W2 < 6.7$), which shown as red dots. Unsaturated stars are shown in black. In the upper left panel the blue dashed line shows the $W1$ saturation limit. In the lower left panel, the dashed line devised by Tu & Wang (2013) does not separate C-rich from O-rich AGB stars, but rather saturated from unsaturated ones.

MC2 then defines in equations 2 the de-projected coordinates x' and y' as linear distances (in kpc) from the LMC centre, in the plane of its disc

$$x' = \frac{D_0 \cos i \sin \rho \cos(\phi - \Theta_{\text{far}})}{\cos i \cos \rho - \sin i \sin \rho \sin(\phi - \Theta_{\text{far}})}, \quad (\text{B3})$$

$$y' = \frac{D_0 \sin \rho \sin(\phi - \Theta_{\text{far}})}{\cos i \cos \rho - \sin i \sin \rho \sin(\phi - \Theta_{\text{far}})}, \quad (\text{B4})$$

where D_0 is the distance from Earth to the LMC, 51 kpc, and $i = 34.7$ is the inclination of the LMC disc plane with respect to our line of sight. $\Theta_{\text{far}} = \Theta + 90^\circ$, where $\Theta = 122.5$ is the position angle (PA) of the “line of nodes”, the intersection of the LMC disc plane and the plane of the sky. See the discussion in MC2 as to why Θ differs from the PA of the LMC semi-major axis.

MC2 finally rotate the (x', y') coordinates by the angle Θ_{far} to align them with another set of coordinates in their paper. For our work, this step is not necessary, but we execute it to obtain a map oriented identically to MC2

$$x'' = x' \cos \Theta_{\text{far}} - y' \sin \Theta_{\text{far}}, \quad (\text{B5})$$

$$y'' = x' \sin \Theta_{\text{far}} + y' \cos \Theta_{\text{far}}. \quad (\text{B6})$$

These are the coordinates we plot in the lower left panel of our Fig. 11. We select all C-rich and O-rich stars that fall within a $\sqrt{x''^2 + y''^2} \leq 10$ kpc circle. Their counts are, respectively, $n_C = 1114$ and $n_O = 252$.

APPENDIX C: TABULATION OF MODEL COLOUR TRACKS AND FILTER FLUXES

Equation (1) averages the observed SED of a source or model with the instrument’s total transmission curves, and calibrates the in-band fluxes to an empirical fit for Vega (Wright et al. 2010). Recall that the *WISE* colour between two bands 1 and 2 is defined as

$$W1 - W2 = 2.5 \log \frac{f_2}{f_1} = 2.5 \left(\log \frac{F_2^{\text{src}}}{F_1^{\text{src}}} + \log \frac{F_1^{\text{Vega}}}{F_2^{\text{Vega}}} \right), \quad (\text{C1})$$

$$= (W1 - W2)^{\text{src}} - (W1 - W2)^{\text{Vega}}. \quad (\text{C2})$$

To compute colours, the absolute scale of the SED is irrelevant, because all scales cancel out. However, to allow luminosity-dependent studies using our models, we list in Table C1, together with the Vega-calibrated *WISE* colours, the unnormalised in-band fluxes F_i^{src} of the Dusty models used in Figs 2, 14–17, and 19. The pure Vega in-band fluxes, using the aforementioned empirical fit, are constants. Their values are: $F_i^{\text{Vega}} = 5.576 \times 10^{-13}$, 2.956×10^{-13} , 7.289×10^{-14} , 4.360×10^{-15} for bands $i = 1-4$, in the same units as the models. The Dusty model SEDs are normalized with the bolometric flux, thus for comparison with observational data the reported F_i^{src} values must be multiplied with the true bolometric flux of the source.

The entire tabulations are available as an electronic supplement file `model_tables.dat` to this paper. All physical properties of the models are listed in the header of each table, and are tabulated in the electronic file. They are: the shell radial optical depth at visual ($0.55 \mu\text{m}$), the dust chemistry, grain size distribution, the

Table C1. Tabulation (excerpt) of *WISE* colours and filter-averaged fluxes F_i^{src} for all *DUSTY* shell model tracks shown in Figures 2, 14, 15, 16, 17, and 19, as a function of the shell radial optical depth at visual (left column). The entire tabulations are available as an electronic supplement to this paper (`model_tables.dat`).

τ_V	...	W1 – W2	W2 – W3	W3 – W4	F_1^{src}	F_2^{src}	F_3^{src}	F_4^{src}
...	...	[3.4-4.6]	[4.6-12]	[12-22]				
...			
# Fig = 12, Ts = 14454 K, dust = ISM, grain_size = MRN, Td = 600 K, density_law = 1/r^0.0								
# 0	...	7	8	9	10	11	12	13
0.000e+0	...	5.780e-3	1.541e-2	1.303e-2	2.102e-3	1.114e-3	2.640e-4	1.779e-5
1.000e-4	...	6.098e-3	2.228e-1	1.769e+0	2.102e-3	1.114e-3	3.196e-4	1.085e-4
...			

photospheric temperature T_s of the central star, the radial density distribution (either a power-law r^{-p} , or RDW), and the dust temperature T_d at the inner radius of the shell. All models have radial shell thickness $Y = R_{\text{out}}/R_{\text{in}} = 100$.